Microfluidics and Nanofluidics (2021) 25:39
https://doi.org/10.1007/s10404-021-02435-w

REVIEW

Pressure measurement methods in microchannels: advances and applications

Feng Shen[1,2,3] · Mingzhu Ai[1,2] · Zonghe Li[1,2] · Xinran Lu[1,2] · Yan Pang[1,2,3] · Zhaomiao Liu[1,2,3]

Received: 17 December 2020 / Accepted: 2 March 2021 / Published online: 6 April 2021

Abstract
With the continuous development of the lab-on-a-chip studies, pressure measurements in microchannels have become the guarantee of the precise control and regulation of trace fluids using microfluidics and caused more research attention. In this review, we first present the basic principles and structures of various pressure measurement methods in microchannels, including the following: (i) membrane or diaphragm-based methods; (ii) membrane-free in-situ methods; (iii) membrane-free side-channel methods; and (iv) other methods. We then illustrate the key applications of these methods in biology, medicine, microfluidic chips, and fluid mechanics. Finally, we prospect the future developments of these methods, which can lead to an unprecedented capability to develop more novel designs of pressure sensors and further applications. We aim to provide a deeper fundamental understanding of the mechanisms of these methods, which could be both a reference for pressure measurement method researchers and a resource for those outside this field who wish to identify the most suitable pressure sensor for a particular application.

Keywords Microfluidics · Pressure sensors · Applications · Diaphragm-based sensors · In-situ methods

1 Introduction

With the development of microfluidics, lab-on-a-chip or micro total analysis systems (μTAS) have been widely used in many applications, such as clinical diagnostics on human physiological fluids, cell biology, detection of tumor cells, biochemical detections, DNA analysis, single-cell trapping, and droplets microfluidics (Li et al. 2015; Sackmann et al. 2014; Schonbrun et al. 2010). Microfluidics is referred to as the science and technology that deals with the precise control and manipulation of traces fluids and particles at microscopic scales (10^{-5}–10^{-3} m) (Whitesides 2006). Pressure distribution is an important fluid dynamic parameter for investigating fluid flow characteristics and optimizing microfluidic chip designs. Any flow has two physical quantities: velocity and pressure field. The velocity characteristics can be measured using a micro particle image velocimetry (micro-PIV) system, which tracks the path of seeded tracer particles to plot flow velocity vector fields. However, this technique can not provide any information about the complementary pressure field, which is essential to fully understand the underlying fluid dynamics (Stone et al. 2004). Therefore, novel pressure measurement techniques are crucial for further developments of microfluidic devices.

The microscale flow in microfluidic chips is driven by conventional pressure methods or by other new methods, such as electromagnetic field effect or gravity, where the fluid motion is essentially caused by the pressure gradient. In particular, for the fluid transportation involved in the fields of chemistry, human physiology, and microfluidic chips, it is necessary to clearly understand the pressure distribution in the flow fields, such as the capture of circulating tumor cells (CTCs) in a microfluidic chip (Khabiry et al. 2009; Shen et al. 2021), the fusion and splitting of droplets (Wang et al. 2021), and the movement of bubbles (Garstecki et al. 2004; Günther and Jensen 2006). In the design of microfluidic

✉ Feng Shen
shenfeng@bjut.edu.cn

✉ Zhaomiao Liu
lzm@bjut.edu.cn

[1] Faculty of Materials and Manufacturing, Beijing University of Technology, Beijing 100124, China

[2] Institute for Advanced Mechanics in Engineering, Beijing University of Technology, Beijing 100124, China

[3] Beijing Key Laboratory of Advanced Manufacturing Technology, Beijing University of Technology, Beijing 100124, China

chips, the hydrodynamic performance of the designed chips is directly determined by the fluid pressure.

Since the early experiments of Poiseuille more than two centuries ago (Sutera and Skalak 1993), the craft of measuring flow fields in tubes and pipes has been perfected. Even so, with the development of micron- and nanometer-scale measurement technology, the resolution limits of these exquisite experimental probes have been approached. As the characteristic dimension of the conventional pressure measurement instruments is already comparable with the size of the microsystems, it is not realistic to apply these techniques to microsystems (Squires and Quake 2005). Unlike the macroscopic scale, the microscale flow with a characteristic scale of 1 μm–1 mm is usually laminar due to the extremely small Reynolds number (*Re*), where the inertial force tends to be very small while the friction, electrostatic force, and intermolecular force become significant (Lissandrello et al. 2012). The microscale structures make the fluid flow and transport more complicated (Schoch et al. 2008). Moreover, many factors such as material and surface characteristics and fluid properties will also affect the microscale flow behaviors. Therefore, there are many challenges in accurately measuring the pressure distribution in microfluidic chips. It is hard to accurately describe the pressure of microscale flows through unified methods, whether it is theoretical analysis, simulation, or experimental exploration.

Although the tools of macroscopic fluid mechanics may not easily be scaled down, the materials and techniques of microfluidics offer unique measurement approaches. Most microchannels in lab-on-chip systems, for instance, are made up of flexible materials (Gervais et al. 2006; Whitesides and Stroock 2001). Polydimethylsiloxane (PDMS) is often the chosen material as it is cheap, transparent, biocompatible, and easy to use (Whitesides et al. 2001; Quake and Scherer 2000). This provides the possibility of probing a flow by monitoring the response of the confining microchannel to the flow pressure.

Recently, many researchers have proposed various methods for measuring the pressure in microfluidic channels and even in nanochannels. According to the different action modes of the pressure sensor's sensitive components, these methods can be roughly classified into four types: (i) thin-film or diaphragm-based methods; (ii) membrane-free in-situ methods; (iii) membrane-free side channel methods, and (iv) other methods (Fig. 1). Currently, the type of setting a thin film or a diaphragm in a microchannel is more commonly used. As the pressure of a fluid flow deforms the film, the pressure at the point of the film can be measured by detecting the strain of the thin film. According to how the deformation of the film is measured, the kinds of pressure sensors can be further divided. For example, the optical sensor uses the optical method to measure the deformation of the film and obtain the pressure value through post image processing. The piezoresistive sensor and capacitive sensor use the electrode resistance or capacitance caused by the deformation of the thin film to characterize the pressure, respectively. The sensor based on the grating diffraction structure can measure the change of the grating pitch and convert it into the pressure variation.

Moreover, according to the location of the sensor elements, the membrane-free methods can be simply divided into two categories, namely in-situ methods and side channel methods. The sensor elements of the first category are directly embedded in the microchannel, e.g. pressure-sensitive paint (PSP) methods, laser interference methods based on image processing, pressure-sensitive conductive gel-based piezoresistive method, deformable microballoon-based colorimetric method and corner rivulets-bubble-based electrical resistance method, while the second category uses a one end-sealed side channel as a sensor, which is connected to the microchannel at the location where the pressure needs to be measured. The pressure in the main channel traps gas into the one end-sealed side channel, causing the change of a gas–liquid interface. The amount of the displacement of the gas–liquid interface caused by compressed gas and applied pressure, therefore, is then interpreted through a system of the ideal-gas-law-based, optical or capacitive sensing.

Furthermore, there are other novel methods that use the pressure difference of laminar flows to achieve in-situ pressure measurement, such as displacement of trapped bead in narrower side channel methods, laminar flow distribution methods based on reference flow, bypass coflowing stream methods, and displacement of interface in twin channel methods. Overall, these methods use ingenious device designs to provide opportunities for dynamic measurement of pressure properties of fluids in very small volumes for different applications.

In this review, we first present a comprehensive review of the recent progress of the pressure measurement methods in microchannels according to the types and action modes of the sensitive element, which is the most crucial part and determines the principle and performance of the pressure sensors. We then illustrate the key applications of these methods in biology, medicine, microfluidic chips, and fluid mechanics. Finally, we discuss the limitation of current studies and prospect several future directions. We hope that this review could serve as a comprehensive guide for readers who are new to the pressure measurement methods. For readers with a decent background, we hope that the review can provide an extended understanding of the fundamental mechanism, inspire novel device designs or initiate expanded applications of pressure measurement methods.

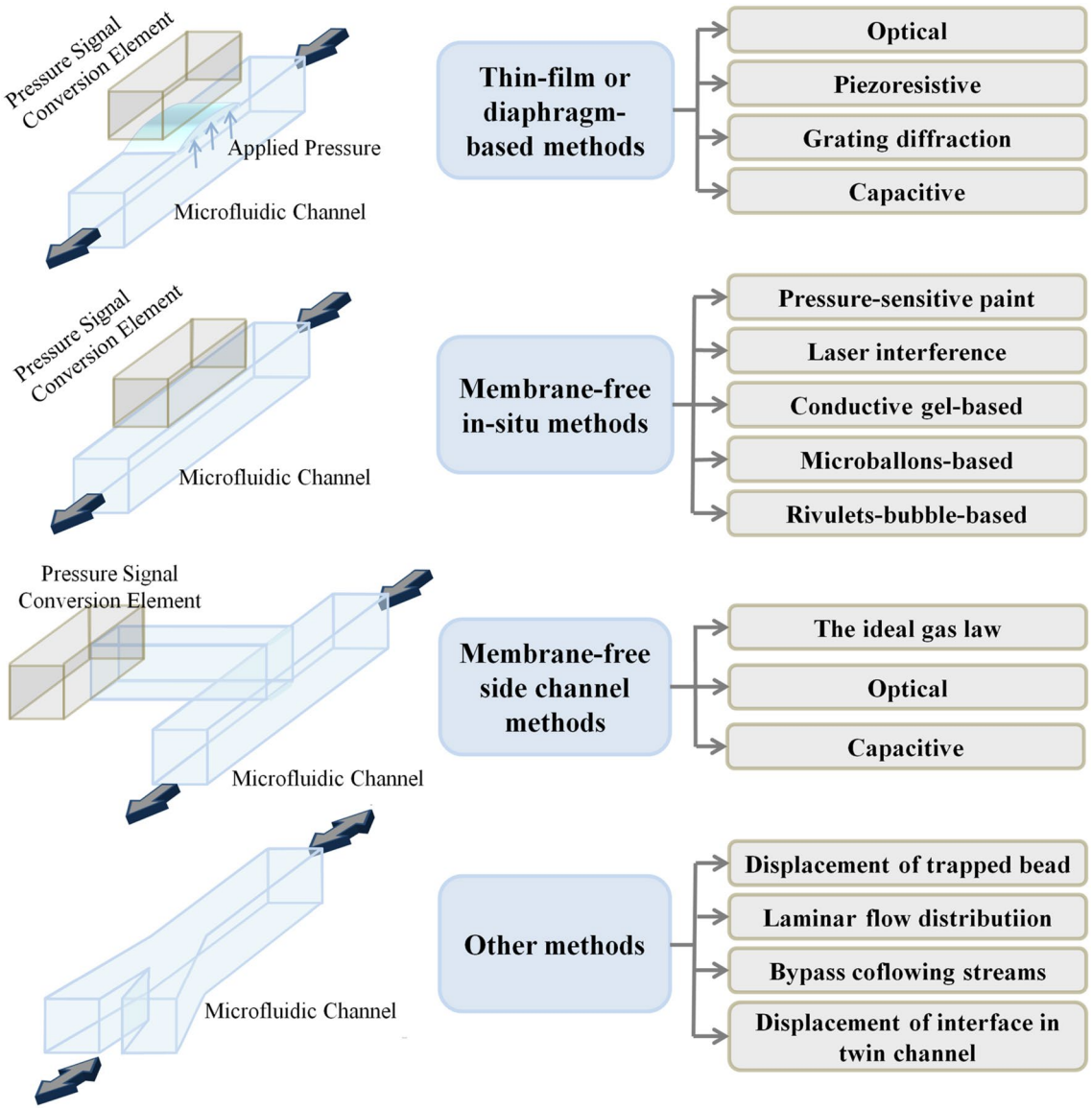

Fig. 1 Classification of pressure measurement methods in microchannels according to the sensor elements

2 Principle of pressure measurement methods in microchannels

2.1 Thin-film or diaphragm-based methods

Most sensors share the common characteristic of a deformable thin-film or diaphragm. The thin-film or diaphragm-based sensors are the most common methods. The pressure of the liquid flow in the microchannel causes the deformation of the membrane fabricated on the wall surface of the microchannel. The membrane deflection can be quantified into a pressure value by various pressure signal conversion elements. According to the operating principle of the sensing elements, these methods can be subdivided into the following types.

2.1.1 Optical methods

The pressure-induced deformation of the thin film embedded in the channel wall can be characterized through optics technology. In recent years, the combination of microfluidics and micro-optics has resulted in a variety of easy-to-fabricate, low-cost pressure microsensors (see Table 1 for a summary of these methods). For example, The pressure sensing element of a membrane-based optical pressure sensor (Molla et al. 2011) is a 100 μm-thick membrane (i.e. the bottom wall), which is fabricated using multilayer soft lithography

Table 1 Optical methods for thin-film or diaphragm-based pressure sensors

References	Characterization methods	Parameters of the film	Size of devices	Range of measurement	Sensitivity	Response time
Molla et al. (2011)	Chromatic confocal microscopy	100 µm-thickness PDMS bottom wall	2 mm in diameter	910–2946 kPa	40 kPa	NA
A line of pneumatically turnable microlenses (Orth et al. 2011)	Microlenses image under a transmission microscope	6.5 µm-thickness PDMS membrane	40 µm in diameter	2–15 PSI	< 10 mPSI (dynamic range of 2.00 PSI)	3 s
A image contrast based sensor (Chaudhury et al. 2016)	Z-scan module	10 µm-thickness PDMS membrane	NA	0–100 mbar	2 mbar (0–20 mbar); 10 mbar (20–100 mbar)	11 s
A vision-based on-chip sensor (Tsai and Kaneko 2016)	Color intensity	500-µm radius deformation chamber	1000 µm in diameter	0–100 kPa	16 Hz	3 s
An integrated OMI (Song and Psaltis 2010a, b, 2011)	Interferometry	530 µm-thickness PDMS membrane	$200 \times 480\ \mu m^2$	0–10 PSI	±2% of full scale	NA
Fluorescence confocal microscopy (Chung et al. 2009)	Image analysis of in-focus particles	15 µm-thickness PDMS membrane	160 µm in diameter	0–10 PSI	0.01 kPa	< 0.25 s
An integrated optical sensing platform (Escudero et al. 2019)	The white light diffraction	50 ± 2 µm-thickness elastomeric on-side nanostructured membranes	1.5 mm in diameter	− 1–1 kPa	$0.17\ kPa^{-1}$	NA
Composite membrane sensing system (Choi and Shim 2019)	Optical intensity	PS-PDMS composite membrane	400 µm in diameter	0–60 PSI	O (10^{-2}) PSI	NA

(MSL) (Freitas et al. 2019; Unger et al. 2000) by etching a 500 µm-thick silicon substrate to a depth of 400 µm at the bottom of a 2 mm-diameter cavity. The cavity is connected to a microchannel through a small channel, whose volume change under pressure manifests deformation of the membrane outwardly. The deformation can be detected using a confocal chromaticity sensor, which uses spectral interferometry and chromatic confocal microscopy to measure the relative membrane deformation with an accuracy of 60 nm. The confocal sensor was focused on the cavity center where maximum deformation occurred. Ten equally spaced membranes were employed to measure the pressure drop along a long serpentine microchannel (80 mm). Each membrane needs to be calibrated separately using a constant hydrostatic pressure before testing. The measured pressure range is 910–2946 kPa with an accuracy of 40 kPa.

Similarly, Orth et al. fabricated a line of pneumatically turnable microlenses to probe the local pressure in a microchannel (Orth et al. 2011), as depicted in Fig. 2a. The straight microchannel is modified to contain many protruding pressure taps, each of which ends with a circular dead end for housing the pressure-sensing microlens membrane. The fluid pressure (P_f) in the microchannel deforms the membrane towards the depression cavity, which contains sealed air (P_{atm}) in the third slide, forming the microlens. The microlens (thickness of 6.5 µm, diameter of 40 µm, and Young's modulus of 700 kPa) is formed by a thin layer of PDMS film bulged by the local pressure. Many small white light-emitting diodes (LEDs) were placed under the microlens. The intensity of the focal spot of each lens is related to the deforming pressure by using a family of calibration curves. In this manner, pressure can be spatially resolved at discrete locations along a microfluidic chip with high sensitivity, fast response time (about 3 s), low noise, and a wide dynamic range that can vary from 2 lb per square inch (PSI) up to at least 15 PSI. These sensors, inexpensive to incorporate into microfluidic chips and easily calibrated and readout, however, require careful calibration and post-processing of the images.

An image contrast-based pressure sensor also includes a sealed pressure microchamber (Chaudhury et al. 2016), whose top and bottom surfaces consist of a 10 µm-thick PDMS membrane and a rigid glass substrate, respectively. When pressure in the chamber increases, the top PDMS film

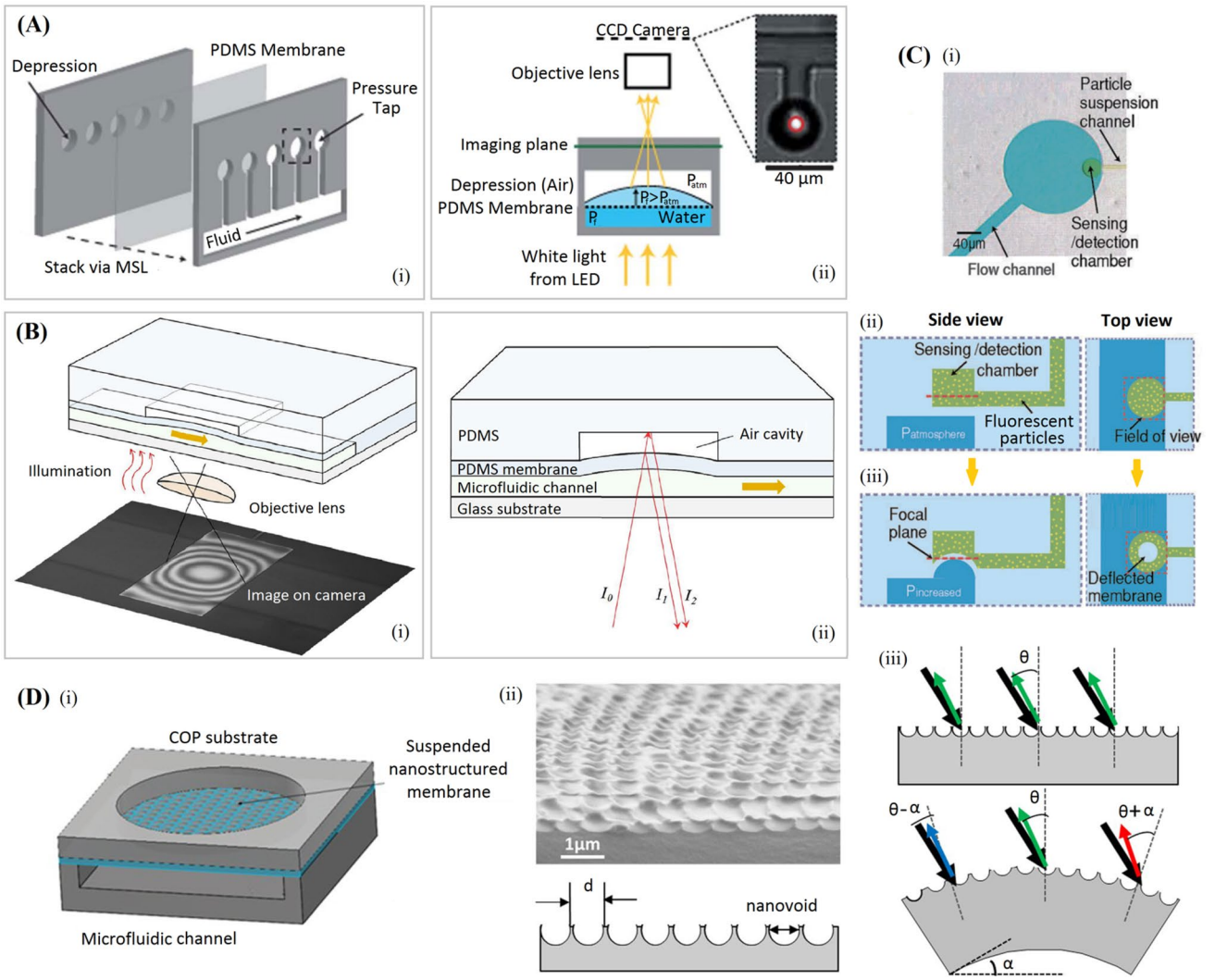

Fig. 2 **a** (i) Schematic of the multilayer PDMS pressure sensor; (ii) geometric structure and micrograph of the sensitive element illustrating the transmission microscope optical path. The red circle indicates the optical intensity averaging region (Orth et al. 2011). **b** (i) The schematic of the whole apparatus of an optical flow control thin-film interferometer (OMI) for pressure measurement; (ii) the operating principle of the OMI (Song and Psaltis 2010a, b, 2011). **c** Design and operating mechanism of the pressure sensor based on fluorescence confocal microscope. (i) Optical micrograph of the sensor; schematic of the cross-sectional views and the top views at a particular focal plane before (ii) and after (iii) applying pressure in the fluidic channel, showing membrane deformation as a function of applied pressure (Chung et al. 2009). **d** (i) Scheme of the multiple optical fluid pressure sensing platform; (ii) scanning electron microscope (SEM) images of the voids leaved on the PDMS; (iii) schematics representation of the membrane bending and the two possible contributions to the change of the reflective color (Escudero et al. 2019)

deforms outwards inducing the increase of the height of the upper and lower surfaces. An objective image, CCD camera, white light source, and Z-scan module were used to obtain the pressure value using a customized image contrast algorithm. The operating pressure range is from 0 to 100 mbar, with a 2-mbar resolution in 0–20 mbar pressure range and 10 mbar resolution in 20–100 mbar pressure range. The measured maximum error is less than 7% throughout its dynamic range. This method requires no electronic components and, therefore, requires no power supply, so it can be used in various biomedical applications as well as in the consumer electronics industry. However, as the PDMS film deviation of different sensors will be slightly different, different sensors need to be calibrated separately to maintain the accuracy and performance.

By fabricating two concentric chambers on a single deformable PDMS layer, Tsai and Kaneko proposed and evaluated a vision-based on-chip sensor (Tsai and Kaneko 2016) for sensing local pressure inside a microfluidic device. The outside big chamber is used as the deformation chamber, while the another inside small one is used as the sensing chamber, which is prefilled with colored fluid. When

pressure is guided into the deformation chamber through a probe channel, it deforms as a result of pressure changes. The deformation in the sensing chamber causes the colored fluid flowing in or out of the chamber and leads to the different color intensities from the top view through a microscope. The sensor can identify the sinusoidal pressure signals up to 16 Hz by using a general 60 frames per second (fps) camera in dynamic tests, and the pressure measurement range is 0–100 kPa. The proposed sensor can directly place the concentric chamber design next to the place to be measured and connect the probe channel to the point of interest. Due to its single-layer design, the sensor can be easily applied to different microfluidic systems such as microfluidic culture environments, to monitor the pressure conditions during culture.

Moreover, beam deflection or interferometry can also be used for optical measurement. For example, Kohl et al. detected the deflection of an internal 50 µm-thick pressure-sensing membrane of a microchannel by utilizing the optical lever technique with an off-chip optical system (Kohl et al. 2005), which involves directing a collimated light source at the membrane and observing the deflection of reflected angle. The integrated optofluidic membrane interferometer (OMI) (Song and Psaltis 2010a, b, 2011) has further achieved technical improvements (Fig. 2b). A flexible air-gap optical cavity (with a thickness of 530 µm PDMS membrane) forms an interference pattern with regular changes under the irradiation of monochromatic light. These interference patterns were captured with a microscope and analyzed by computer using a pattern recognition algorithm. A dynamic range of 0–10 PSI with an accuracy of ± 2% of full scale was obtained. By changing the thickness of the film, the sensitivity, and working range of the pressure sensor can be adjusted. The researchers declare that as the fabrication of the sensor is fully compatible with PDMS-based microfluidic chips and has a small footprint, the entire sensing unit can be integrated into other microfluidic chip for in-situ pressure measurement at one or multiple locations.

In addition, fluorescence confocal microscopy can provide a simple and economical alternative optical method (Gervais et al. 2006). For instance, the sensor shown in Fig. 2c consists of two chambers in two bonded PDMS layers and a thin membrane between them (Chung et al. 2009). The upper chamber is used as the detection chamber prefilled with a suspension of fluorescent particles. The focal plane of the confocal microscopy is positioned at the deformable membrane. The pressure change in the lower chamber connected with the flow channel will cause the membrane to deflect towards the upper detection chamber. The cross-sectional area of the focal plane can be quantified as a function of applied pressure. By adjusting the distance of the focus plane, the dynamic range of this sensor can be adjusted, which varies from 0 PSI up to 10 PSI. With its small size, this sensor can be easily integrated with microsystems, and pressures in multiple positions can be measured simultaneously.

The above sensors are based on monitoring the deformation of an embedded membrane within a microcavity. On the contrary, in recent years, some novel sensors using material modification of the outside surface of a thin film to perform pressure monitoring have also been reported. Escudero et al. developed an integrated optical pressure sensing platform (Escudero et al. 2019) for multiplexed optofluidics applications. The platform consists of an array of elastomeric on-side nanostructured membranes (Fig. 2d), which will present color shifts in response to mechanical stresses that alter their nanostructure characteristic dimensions, pitch or orientation. The pressure–color relationship can be evaluated via UV–Vis reflection spectrometry. The pressure measurement range is − 1–1 kPa with a maximum achievable sensitivity of 0.17 kPa^{-1}, while higher sensitivity can be achieved by adjusting the film size and PDMS thickness.

Furthermore, instead of using a thin PDMS film, Choi and Shim fabricated a novel composite membrane as the pressure sensing film (Choi and Shim 2019), which is composed of self-assembled polystyrene (PS) colloidal crystals and flexible PDMS matrix. The composite membrane, which exhibits angle-sensitive reflection colors, can be integrated directly into the microfluidic device. The sensitivity and sensing range can be varied based on the geometrical design of the composite membrane. The sensing range is limited by the bonding strength of PDMS. For example, the sensing range can reach 0–60 PSI when the width of the microchannel is 25 µm. The sensitivity of the colloidal crystal membrane is O (10^{-2}) PSI, which can be further enhanced by using thinner membrane.

2.1.2 Piezoresistive methods

Among many silicon-based microsensors, piezoresistive pressure sensors are one of the most successful application products of the microelectromechanical systems (MEMS) technology. Piezoresistivity is a material property, and the electric resistance of the material is influenced by the applied mechanical stress. Piezoresistive effects of silicon or germanium are commonly used for piezoresistive pressure sensors (Maroufi et al. 2020; Setiono et al. 2020). The basic structure of a piezoresistive pressure sensor consists of a thin silicon diaphragm with four diffused sensing piezoresistors in a closed Wheatstone bridge configuration (Park et al. 2007). When pressure is applied, the mechanical force on the sensing element (a thin membrane or diaphragm) results in its deformation, which changes the resistance and electrical output of the sensor (Jung and Yang 2015; Lee and Choi 2008; Park et al. 2007; Wang et al. 2009; Wu et al. 2011, 2012). Compared with other types of pressure sensors, piezoresistive sensor provides several advantages, such as mechanical

stability due to its lightweight and small size, inherent high gauge factors, and low output impedance. Many elaborate piezoresistive sensors have been proposed to measure pressure in microfluidic chips (see Table 2).

By replacing silicon wire with a carbon fiber, and performing backside etching on silicon-on-insulator wafer, a carbon fiber-based piezoresistive sensor is formed (Park et al. 2007), as shown in Fig. 3a. The pressure in the cavity causes deformation of the upper thin membrane, which will apply mechanical stress on the carbon fiber. The carbon fiber was aligned and deposited across the gap (150 μm) between two Cr/Au electrodes using dielectrophoresis. Compared with silicon wire, carbon fibers are easier to be fabricated and have higher gauge factors. The pressure range is determined by the types and sizes of the carbon fibers. Differently, using a 50 μm-thickness PDMS diaphragm instead of a silicon diaphragm, Lee and Choi developed another carbon fiber-based piezoresistive sensor (Lee and Choi 2008), whose sensing range is 0–0.25 bar. Through their investigation, it is confirmed that due to the lower Young's modulus, PDMS diaphragm can provide higher sensitivity than silicon-based pressure sensor.

Thanks to the piezoresistive effect of different conductive media, many researchers have invented a variety of self-sensing films, which can be integrated into microfluidic devices as a new type of micropressure sensor. Among them, conductive materials such as carbon nanomaterials (Toan et al. 2018) and SiC wafers (Phan et al. 2018) are used as sensing elements. Carbon nanotube (CNT) yarn embedded in elastomers (Fig. 3b) show high potential as an advanced functional element for a wide range of mechanical sensing applications including flexible pressure and tactile sensing. The decrease of CNT resistance with increasing pressure is attributed to the increase in the volume fraction of CNT, resulting in the increase of the effective junctions between adjacent CNTs, and the reduction of the tunneling distance between single CNTs. The compact and lightweight CNT yarns were fabricated using heat treatment and aligned by the capstan rod system, showing a high potential for pressure sensing where the applications of pressure threshold lower than 60 kPa are applied, and the pressure sensitivity was found to be approximately 4.7×10^{-4} kPa for the CNT yarns. Also the self-sensing SiC membrane with metallic Ni electrodes is formed by applying lithography and plasma etching techniques to a 100 nm-thickness SiC film. The principle of the self-sensing membrane is based on the piezoresistive effect of the SiC film, which utilizes the change of the SiC resistance under mechanical impacts. The sensors exhibit excellent linear response to the applied pressure, as well as good repeatability.

Table 2 Piezoresistive methods for thin-film or diaphragm-based pressure sensors

References	Parameters of the film	Size of devices	Range of measurement	Sensitivity	Response time
A carbon fiber-based piezoresistive sensor (Park et al. 2007)	9 μm-thick silicon diaphragm	1.5×1.5 mm^2	Determined by the types and sizes of the carbon fibers	Due to the lower Young's modulus, PDMS diaphragms can provide higher sensitivity than silicon-based pressure sensors	NA
A carbon fiber-based piezoresistive sensor (Lee and Choi 2008)	50 μm-thick PDMS diaphragm	500×500 μm^2–1000×1000 μm^2	0–0.25 bar		NA
Toan et al. (2018)	500 μm-thickness acrylic elastomer embedded with CNT yarn	2.5×2.5 cm^2	0–60 kPa	4.7×10^{-4} kPa^{-1}	NA
Self-sensing SiC membrane (Phan et al. 2018)	Free-standing SiC sub 100 nm-thick membranes	300×350 μm^2	0–1.6 bar	NA	NA
Wang et al. (2009)	20 μm-thickAg/PDMS conducting composite	NA	0–100 kPa	0.01 kPa	100 ms
PorousPDMS foam-based sensor (Wu and Li 2020)	Porous PDMS foam embedded with graphene	NA	0–100 kPa	17.9 kPa^{-1} (0–30 kPa) 79 kPa^{-1} (30–100 kPa)	20 ms
Tactile diaphragm sensor based on Galinstan (Jung and Yang 2015)	PDMS-based microchannel filled with galinstan	$800\times600\times20$ μm^3	0–12 kPa with 230 kPa as the limit	$R^2>0.999$	NA
Liquid metal pressure sensor based on Galinstan (Gao et al. 2017)	PDMS-based microchannel filled with Galinstan	70×70 μm^2	0–50 Pa with 100 Pa as the limit	0.0835 kPa^{-1}	90 ms
An electrofluidic circuit based sensor (Wu et al. 2011, 2012)	100 μm-thick PDMS membrane	<1 mm^2	0–40 PSI	$R^2>0.998$	4 s

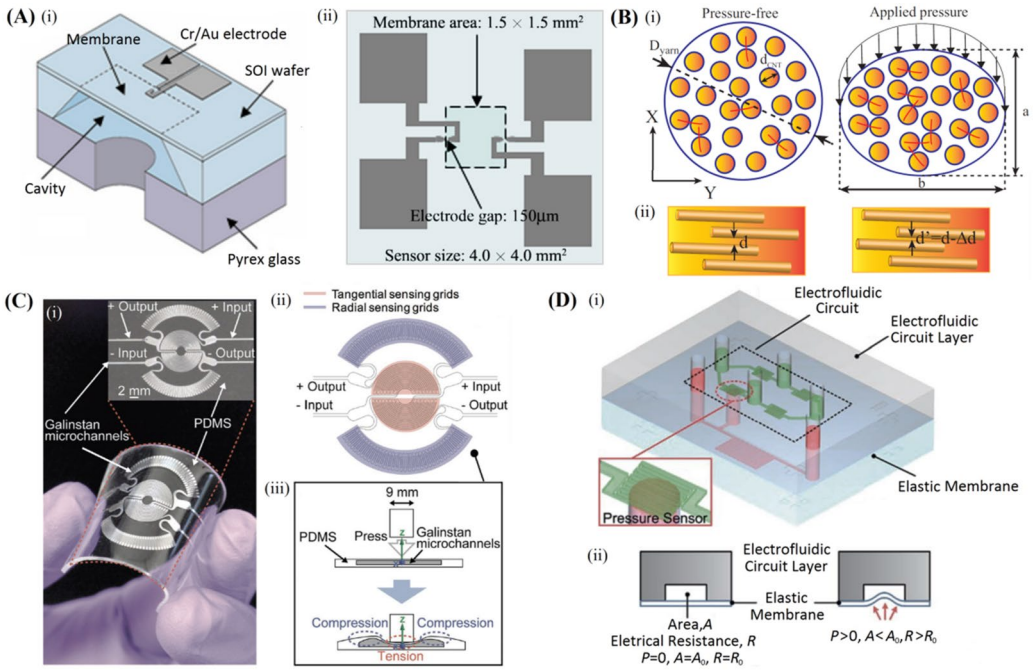

Fig. 3 **a** Schematics of the carbon fiber-based piezoresistive pressure sensor for measuring the membrane deformation (i) cross section view; (ii) top view (Park et al. 2007). **b** Schematic sketch of the pressurising effect on the CNT junctions. (i) Pressurising effect increases the number of effective CNT junctions. (ii) Pressurising effect on the tunneling distance between CNTs in CNT junctions (Toan et al. 2018). **c** Microfluidic tactile diaphragm pressure sensor. (i) Optical image of a finished microfluidic diaphragm sensor. (ii) Schematic layout of the diaphragm sensor and (iii) a schematic diagram indicating testing conditions (Gao et al. 2017). **d** Illustration of the electrofluidic circuit-based pressure sensor. (i) The schematic of the system with a PDMS membrane sandwiched by two PDMS layers: microfluidic channel and electrofluidic circuit layers; (ii) the working principle of the integrated pressure sensor converting mechanical pressure to electrical resistance variation (Wu et al. 2011, 2012)

In addition, Wen's research group has reported a flexible strip fabricated of Ag/PDMS conducting composite (Wang et al. 2009), i.e. a mixture of microsized granules of silver powder and PDMS gel. The composite strip works as the sensing element, replacing the carbon and electrodes, and can produce electrical signals directly. The response time of this sensor is approximately 100 ms within a sensing range as wide as 0–100 kPa. The resolution can reach 0.01 kPa and the accuracy of the testing device is 0.5 kPa. Graphene, as a material that can be produced on a large scale at low cost, also has good electrical conductivity. The flexible pressure sensor (Wu and Li 2020) using graphene as raw material and porous PDMS foam as membrane matrix can have a wide range of application potential in the biomedical field (such as wearable devices): it is provided with fast response ability (20 ms), and the high elastic modulus of PDMS gives the sensor a wide pressure response range (0–100 kPa), while controlling the amount of graphene loaded gives the sensor high sensitivity (the average sensitivity in the range of 0–30 kPa is 17.9 kPa^{-1}, the sensitivity in the range of 30–100 kPa reaches 79 kPa^{-1}), and device stability (more than 10,000 cycles) (Jung and Yang 2015). A novel liquid metal pressure sensor based on Galinstan (Jung and Yang 2015) is developed by Sung's team, the pressure sensor-integrated microfluidic device consists of three PDMS layers. Among them, the sensor layer contains microchannel filled with galinstan, which works as the sensing element. When the membrane layer is subjected to pressure, due to the reduction of the cross-sectional area of the galinstan-filled microchannel, the electrical-resistance in the pressure sensor increases. Since Gelinstein exists in a liquid phase at room temperature (20 °C), this sensor can be easily integrated into various microfluidic systems for long-term pressure monitoring with high linearity ($R^2 > 0.999$, within a pressure range from 0 to 230 kPa), repeatability, and long-term stability. Therefore, the proposed pressure sensor can be employed in various microfluidic applications, as well as in microviscometers for stable pressure monitoring. Figure 3c demonstrates another microfluidic tactile diaphragm pressure sensor based on embedded Galinstan microchannels (70 μm width × 70 μm height) capable of resolving sub-50 Pa changes in pressure with sub-100 Pa detection limits and a response time of 90 ms (Gao et al. 2017). An embedded equivalent Wheatstone bridge circuit makes the most of tangential and radial strain fields, leading to high sensitivities of a 0.0835 kPa^{-1} change in output voltage.

The sensor overcomes the problem that the sensor based on liquid metal cannot solve the small pressure change in the few kPa range, making it suitable for applications such as heart rate monitoring, which require a much lower pressure detection resolution.

Different from the above structure, Wu et al. using ionic liquid (IL) filled in microchannels to form a current circuit as the sensing element, designed an electrofluidic circuit-based pressure sensor (Wu et al. 2011, 2012), as shown in Fig. 3d. The integrated sensor is constructed by a glass substrate and two PDMS layers with channel patterns: a microfluidic channel layer and an electrofluidic circuit layer. The two layers are separated by a 100 μm-thick PDMS membrane. A pressure transduction hole is fabricated on the bottom layer and aligned to the electrofluidic channel on the top layer. The electrofluidic channel constructs an equivalent Wheatstone bridge circuit. The integrated pressure sensor can convert the mechanical pressure into electrical resistance variation with the input pressure range from 0 to 40 PSI. This sensor is robust, disposable, and capable of large-scale integration.

2.1.3 Grating diffraction methods

Pressure sensors based on grating diffraction usually embed/connect various grating elements into the deformable membranes on the microchannel wall (Eaton and Smith 1997). As the stress state of the membrane changes, the pitch of the grating will also change, which is then measured using various optical methods, such as chromaticity change and corresponding resonance wavelength, to characterize the pressure (see Table 3).

Hosokawa et al. first presented a grating diffraction-based sensor by carving a deformable 2×2 mm^2 diffraction grating on the bonding interface of a PDMS microchannel plate and a flat glass plate (Fig. 4a) (Hosokawa et al. 2002). The grating consists of 5 μm-wide, 2 μm-deep rectangular grooves arrayed with a period of 10 μm interval and connected to the microchannel. By measuring the intensities of monochromatic diffracted beams as well as the chromatic change of the grating illuminated by white light, the optical response of the sensor to pressure can be detected, which ranges from − 80 to 100 kPa. The authors claim that this method opens up the possibility of producing new types of fiber-optic pressure sensor and pressure-driven optical modulator.

Further, a high-resolution (< 200 mtorr) grating diffraction sensor (Foland et al. 2011, 2012) is based on guided wave mode resonance (GMR) composed of titanium dioxide (TiO_2) nanograting embedded in an 85 μm-thickness PDMS membrane. The embedded GMR grating has a pitch distance of 500 nm when the PDMS membrane is unstrained. When fluid pressure increases, the membrane is strained, resulting in an increase in the grating pitch as well as its corresponding resonant wavelength. The grating has a resonance response at around 727 nm, producing a peak in the reflectivity spectrum of the grating. The sensor is able to detect changes in relative pressure throughout a range of 0–60 torr. Cooksey et al. incorporated a commercially available fiber Bragg grating (FBG) (Xu et al. 2013) into a flexible PDMS membrane and positioned it below a microchannel (Fig. 4b)

Table 3 Grating diffraction and capacitive methods for thin-film or diaphragm-based pressure sensors

References	Parameters of the film	Size of devices	Range of measurement	Sensitivity	Response time
Engraved-based grating diffraction sensor (Hosokawa et al. 2002)	Engraved diffraction grating on PDMS film	2×2 mm^2	− 80–100 kPa	NA	NA
GMR-based grating diffraction sensor (Foland et al. 2011, 2012)	85 μm-thick PDMS membrane embedded with TiO_2 nanograting	750×750 μm^2	0–60 torr	< 200 mtorr	NA
FBG-based grating diffraction sensor (Cooksey and Ahmed 2016)	≈ 180 μm-thick PDMS membrane embedded with a FBG	NA	0–75 kPa	< 700 Pa	NA
A high-precision gas flowmeter (Cho et al. 1992)	2.9 μm-thick stress-compensated diaphragm	2 mm × 2 mm × 2.9 μm	1 mtorr–700 torr	< 0.03 fF mtorr^{-1}	0.7 ms
A capacitive sensor with embedded miniaturized elements (Sekimori et al. 2004)	25 μm-thick Polycrystalline-SiC coating	1 mm^3	0–100 kPa	NA	NA
A droplet-based interfacial capacitive sensor (Nie et al. 2012)	Polymeric membrane coated with transparent conductive materials	18 mm in diameter	2–20 kPa	1.58 μF kPa^{-1}	260 ms
A one-side-electrode-type fluidic based sensor (Nawi et al. 2015)	0.8 mm-thick PDMS diaphragm	40 mm × 25 mm	1–7 kPa	0.77 pF kPa^{-1}	0.12 s

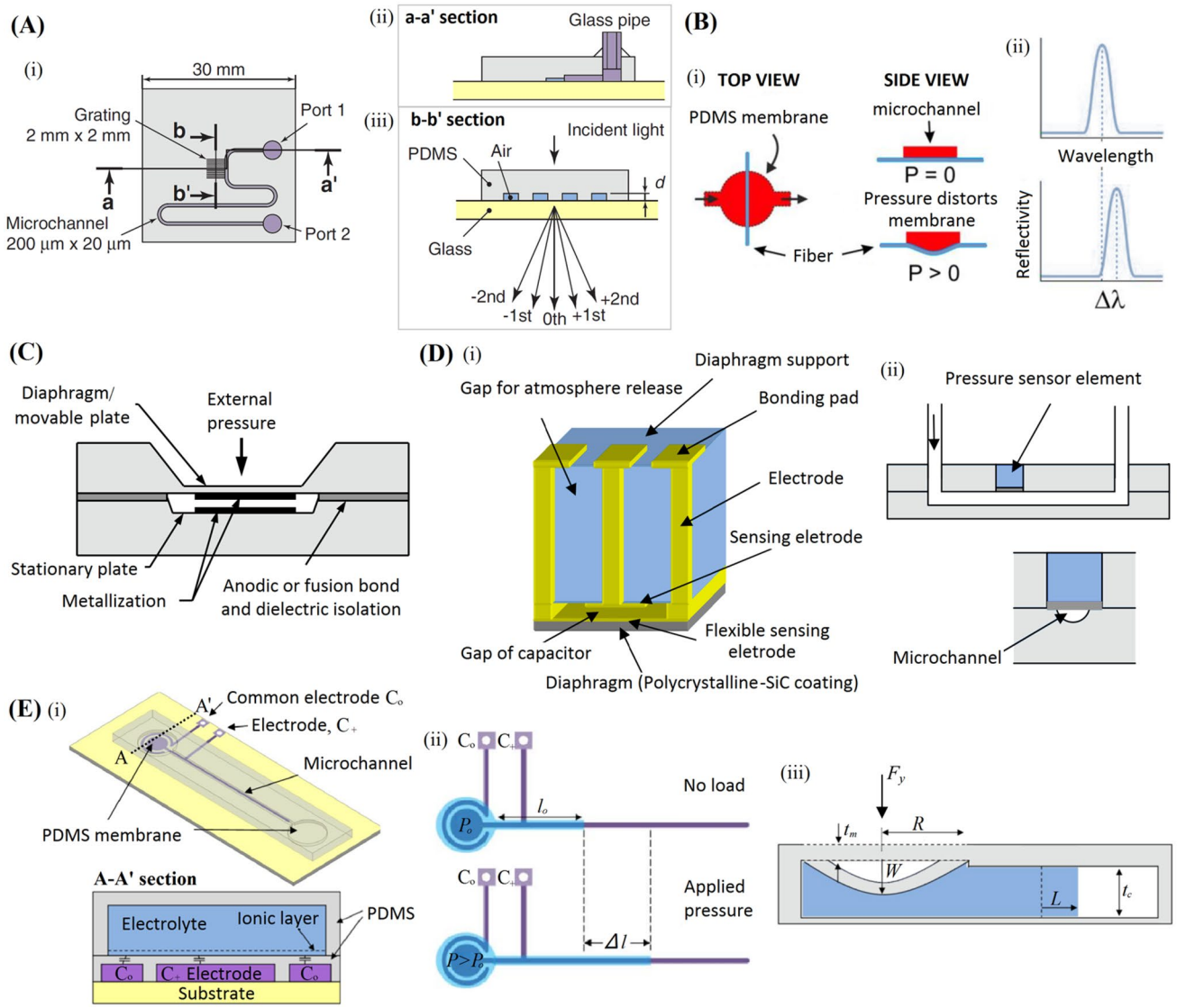

Fig. 4 **a** The layout of the deformable diffraction grating based pressure sensor. (i) Top view; (ii) section a–a′; (iii) enlarged view of section b–b′ (Hosokawa et al. 2002). **b** (i) An FBG (blue) embedded in a flexible membrane responds to strain applied via a microfluidic channel (red) and deflects down into an open chamber; (ii) the green trace depicts the Bragg resonance shift (Cooksey and Ahmed 2016). **c** A cross-section schematic diagram of a bulk-micromachined capacitive pressure sensor. **d** (i) A sectional view of the capacitive pressure sensor; (ii) schematic diagram of cross-section of the position where the sensor is embedded in the microchannel (Sekimori et al. 2004). **e** (i) Side view of the one-side-electrode-type fluidic based capacitive pressure sensor and cross-sectional view of A–A′ section; (ii) sensor pattern for no-load and applied pressure condition; (iii) the cross-section and the fluid mechanism of the sensor (Nawi et al. 2015)

(Cooksey and Ahmed 2016). Pressure causes the deflection of the flexible film to change, which strains the fiber and shifts the Bragg wavelength. The measured fluid pressure ranges from 0 to 75 kPa (0–10.9 PSI), which covers typical pressures for microfluidic applications.

Grating diffraction-based pressure sensors have been shown to exhibit better pressure sensitivity and lower temperature sensitivity than pure piezoresistive sensors. Furthermore, a frequency output is more immune to noise than classical analog piezoresistive and capacitive signals (Bogaerts et al. 2012; Tan and Dai 2018).

2.1.4 Capacitive methods

Capacitive pressure sensors can measure physical quantities such as pressure and convert them into electrical signals in the form of capacitance. Due to the high sensitivity, capacitive sensors have attracted much attention and have been used in many applications, including pressure sensing, flow measurement, and depth sensing (see Table 3). Typically, a typical bulk-micromachined capacitive pressure sensor contains two parallel electrodes (Fig. 4c). One is attached to a deformable diaphragm while

the other one is fixed on stationary plate. When the diaphragm deforms or displaces, the capacitance between the two electrodes changes, which depends on both their distance and contact surface area.

The principal advantages of capacitive sensors over piezoresistive sensors are increased pressure sensitivity and decreased temperature sensitivity (Huang et al. 2005; Sun et al. 2011). Generally, the piezoresistive sensor has a complex transducer with simple circuit requirements, while the converse is true of the capacitive sensor. Therefore, capacitive sensors have benefited more from advances in circuit design than piezoresistive sensors (Lee et al. 2008).

Cho et al. integrated a capacitive pressure sensor with a silicon microchannel to create a high-precision gas flowmeter (Cho et al. 1992). The sensing element is a 2.9 μm-thick stress-compensated diaphragm, which enables the sensor to monitor pressure drop as low as 1 mtorr while withstanding overpressures greater than 700 torr. Furthermore, a capacitive pressure sensor (Sekimori et al. 2004) with embedded miniaturized sensor elements (volume of 1 mm^3) has no interference to the flow during the measurement, as shown in Fig. 4d. The pressure sensor element consists of two electrodes, forming a gap of capacitor between them. The sensor can be installed on a microchip by gluing it into a hole without any dead volume and disturbance to the flow. Then, a circuit of application specific integrated circuit (ASIC) for capacitance measurement is connected, and pressure can be measured. The pressure range is 0–100 kPa and the calibration curve is nearly linear.

Instead of using metalized electrode, a novel droplet-based interfacial capacitive sensor (Nie et al. 2012) uses two membranes with conductive coating to form capacitor electrodes, which can achieve ultrahigh mechanical-to-electrical sensitivity (1.58 μF kPa^{-1}) and resolution (1.8 Pa) with a simple sensor architecture. Due to the high sensitivity and small size, this sensor can be used for wearable pressure measurement systems in some biomedical fields.

Moreover, to overcome the fabrication complexity and further protect the sensor from external pressure, Nawi et al. developed a one-side-electrode-type fluidic based pressure sensor (Nawi et al. 2015), as shown in Fig. 4e. In the cavity filled with electrolyte, an ionic layer forms on top of the insulated PDMS, which will behave as a conductor and generate capacitance. When pressure is applied, the membrane deflection which will push the electrolyte inside the microchannel. The displacement of the electrolyte will result in the changes of the capacitance value between electrodes and can be detected. The response time and sensitivity of the sensor are 0.12 s and 0.77 pF kPa^{-1}, respectively. The test pressure ranges from 1 to 7 kPa and is suitable for applications where low-pressure inputs are monitored, e.g. biomedical applications.

2.2 Membrane-free in-situ methods

Instead of fabrication of a thin deformable membrane/diaphragm, various membrane-free methods have also been proposed. The sensor elements of the in-situ membrane-free methods are directly embedded in the microchannel where the pressure is to be measured. According to the structure and operating principle of the sensor element, this category of methods can be further divided as follows. Studies that provide the membrane-free in-situ method to measure pressure are summarized in Table 4.

2.2.1 Pressure sensitive paint (PSP) methods

PSP is a relatively new technique for surface pressure measurement in aerodynamic experiments. PSP has also been used for pressure measurement inside the fluid flow and wind tunnels (Abe et al. 2004; Kimura et al. 2006). This technique uses luminescence signals emitted from fluorescence molecules to visualize the pressure distribution and has the advantages of straightforward deployment and non-intrusive measurement, providing an alternative way for pressure measurements inside microfluidic devices.

Many researchers have applied the PSP to micro-scale flows, providing detailed pressure distribution for studying the flow fields. The apparatus for PSP experiments in micro-scale includes an excitation light source, a photodetector, selected optical filters, and PSP sensors, which are similar to the conventional measurements in macroscale. A photodetector is used to collect the luminescence emitted from PSP sensors during excitation (Huang et al. 2014). The fundamental operating principle of PSP is the oxygen quenching of paint fluorescence. The light intensity emitted by the paint is inversely proportional to the local air pressure. For the small size of molecular sensors, the general luminophore size is as small as a few nanometers. Therefore, the molecules can be put inside the MEMS devices. Significantly, the molecular sensor can provide global pressure profiles with great spatial resolution as fine as just a few micrometers, with maximum sensitivity in the low-pressure range below 1 PSI, where standard pressure transducers usually have difficulty in making measurements (Liu et al. 1997; Schanze et al. 1997).

Matsuda et al. reported a novel PSP coating method by using Langmuir–Blodgett (LB) technology to manufacture a pressure-sensitive molecular membrane (PSMF) (Matsuda et al. 2009; Yu et al. 2007), which solves the problem where the conventional PSP is too thick owing to the use of polymer binder and does not have sufficient spatial resolution for pressure measurement in microflows. However, because the fabrication of PSMF takes a long time and its application is restricted only to flat chemically modified surfaces, this PSMF method is difficult to be common for practical use.

Table 4 Membrane-free in-situ pressure sensors

References	Sensing elements	Size of devices	Range of measurement	Sensitivity	Response time
PSCC (Matsuda et al. 2011)	PDMS with luminophore layer	NA	12–20 kPa	< 0.04 kPa	NA
Huang et al. (2007)	PSP sensor coating with 1 μm-thickness and 0.06 μm-surface roughness	NA	0.001–30 PSI	5 μm	NA
Huang and Lai (2012)	PDMS-based PSP sensor coating with 10 μm thickness	NA	0.001–50 PSI	3 μm	NA
An off-chip, noninvasive microfluidic sensor (Kamruzzaman et al. 2019)	Interference of the reflected waves from the microchannel	NA	1–10 PSI	NA	NA
A conductive gel-based sensor (Li et al. 2010)	Ni-PDMS conductive gel blocks	30 lm^2	0–1 bar	NA	Few seconds
A droplet-based interfacial capacitive sensor (Banerjee and Mastrangelo 2016)	The deformable microballoons	12–15 μm in diameter	0–25 PSI	0.44 nm PSI^{-1}	5 min
A corner rivulets-bubble (CRs-B) sensor (Tang et al. 2019)	An ultrathin polymer foil with a chamber and two embedded electrodes	$18 \times 100 \times 580$ μm^3	0–200 mmHg	$0.11\% \cdot L_0$ $mmHg^{-1}$	NA

Hence, by combining the PSP with PDMS micro-molding technique, the team further developed a new pressure-sensing device named pressure-sensitive channel chip (PSCC) (Matsuda et al. 2011), as shown in Fig. 5a. Above the microchannels in the PSCC, there are three layers: a sensor layer, a parylene layer, and a PDMS supporting block. The sensor layer is fabricated by PDMS containing a pressure-sensitive luminophore, which works as the PSP, and the parylene layer can prevent oxygen permeation from the sensor layer to the PDMS supporting block, thereby prolonging the service life of the sensor. Pressure distribution in the covered microchannels can be monitored with the sensitivity equalling that of conventional PSP methods. By detecting the pressure distribution of the nozzle, it can be concluded that the error in the PSCC measurement caused by the calibration error is less than 0.04 kPa in the range of 12–20 kPa.

As another method of preparing thin PSP coatings, the spin-coating method can also precisely control the paint thickness, which is used to apply PSP sensor coating on a glass slide, creating a thin and uniform layer with about 1 μm thickness and 0.06 μm surface roughness (Huang et al. 2007). The glass slide with PSP sensor was used as cover glass to seal the straight microchannel with rectangular cross section. The pressure distribution inside the microchannel and the entrance of the channel is obtained, and the pressure measurement range can reach from 0.001 to 30 PSI. This method is able to capture 5-μm resolution pressure maps at the inlet of the channel with the help of a CCD camera. Nonlinear pressure distribution along the channel was observed within the microchannel due to the compressibility effect. Huang and Lai further solved up to 77% of the error by pixel-by-pixel calibration on the CCD chip (Huang and Lai 2012), and each pixel achieved a detailed resolution of up to 3 μm in the local pressure evolution. Taking the advantages of two-dimensional pressure map acquired by the PSP method, the flow pattern after a sudden constriction can be investigated in detail.

2.2.2 Laser interference method

Using the light interferometry, Kamruzzaman et al. introduced an off-chip, noninvasive microfluidic pressure-sensing method (Kamruzzaman et al. 2019), as shown in Fig. 5b. A helium–neon laser beam is allowed to propagate through the fluid-filled microchannel. Then using a high-resolution camera, the interference of the reflected waves from the microchannel is presented as bright/dark fringes and captured for applied pressures of 1–10 PSI. These fringes move or shift positions as a response to the fluid pressure change inside the microchannel. By establishing interplay among fringe shift, index of refraction, and pressure, indirect sensing of the pressure change is possible. It provides a novel opportunity to detect fluid pressure in microscale pores, which precludes directly inserting pressure sensors into such a small space. However, the air current in the environment, stray light, and surrounding vibrations must be strictly controlled, since these parameters can weaken experimental findings. Besides, methodical calibration of the experimental setup should be performed prior to every measurement cycle.

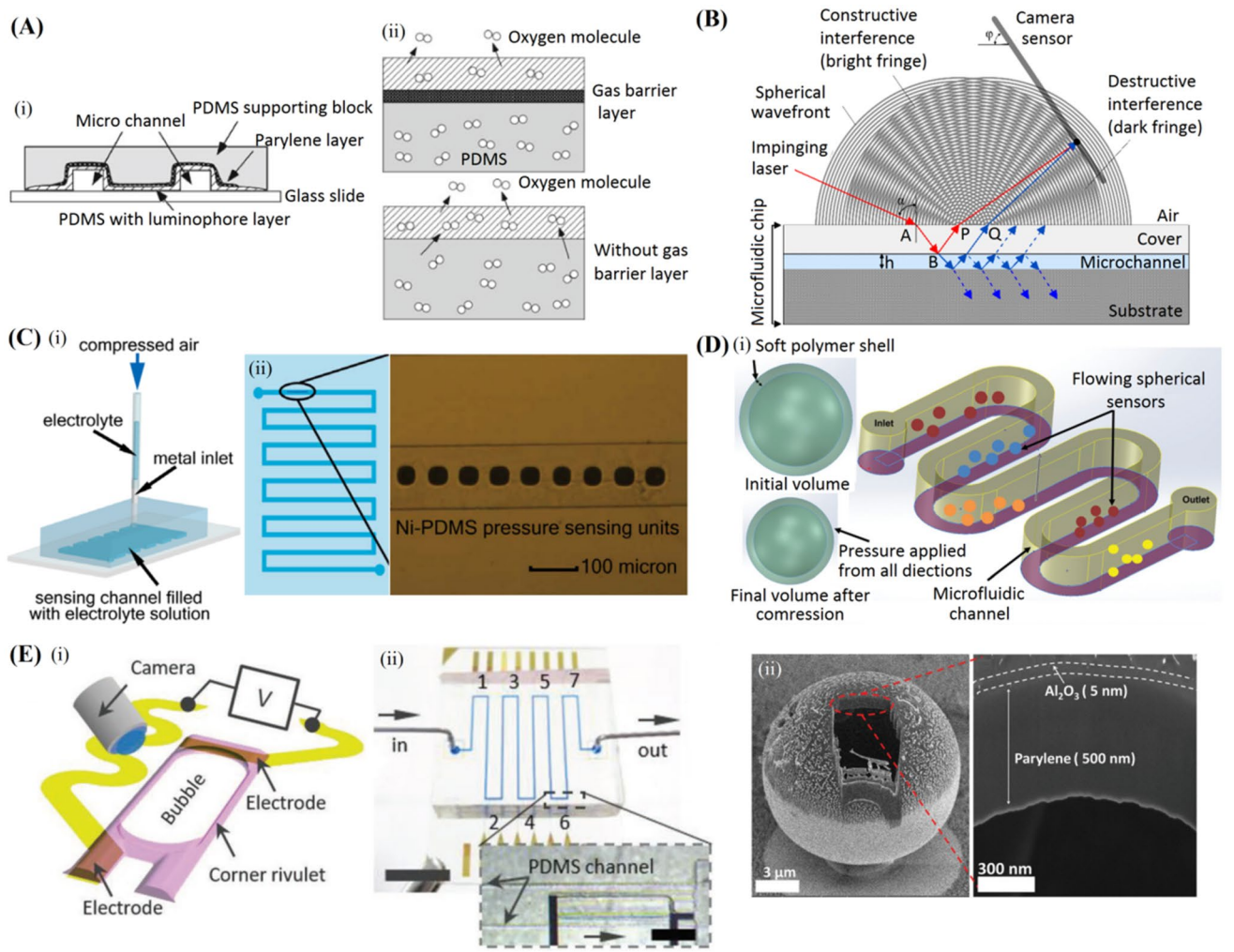

Fig. 5 **a** (i) A schematic diagram of pressure-sensitive channel chip (PSCC); (ii) a schematic showing the effect of the gas barrier layer, which can prevent oxygen permeation from the sensor layer to the PDMS supporting block (Matsuda et al. 2011). **b** The interference and the formation of constructive and destructive fringes as a laser beam impinges on a fluid-filled microfluidic chip (Kamruzzaman et al. 2019). **c** (i) Schematic view of the sensing device: the electrolyte was injected through a metal inlet and the pressure in microfluidic channel was controlled by air pressure applied to the electrolyte; (ii) microphotograph of a Ni-PDMS electrogel array in a microfluidic channel (Li et al. 2010). **d** (i) Schematic showing compression of hollow microballoons under external pressure, which are used for mapping the internal pressure drop within microfluidic chips; (ii) focused ion beam cross-section of one spherical microballoon and the image on the right shows a magnified image of the cross-section delineating the parylene shell and the Al_2O_3 diffusion barrier (Banerjee and Mastrangelo 2016). **e** (i) Illustration of the pressure-sensitive element, and the transduction methods of the sensor; (ii) application of seven sensors distributed along the flow in a microfluidic system. The inset is a bubble formed in a sensor within the microchannel (Tang et al. 2019)

2.2.3 Pressure-sensitive conductive gel-based piezoresistive method

A new type of conductive gel-based pressure sensor (Li et al. 2010) can also achieve real-time in-situ pressure monitoring, whose sensing elements were obtained by casting a viscous mixture of PDMS and metal powders (Ni) on a patterned template, as shown in Fig. 5c. After solidification, the gel blocks become conductive, showing piezoresistive effects, and thus can be used for low-pressure sensing. Here, the electrolyte (saturated potassium chloride solution) was injected for conductivity monitoring between the electrolyte and the substrate, passing through the Ni-PDMS gel blocks. The measured conductivity is correlated to the applied pressure. The pressure sensor elements are small (30 lm^2) and reliable for in situ pressure determination at 0–1 bar in commonly used microfluidic devices. The fabrication process of the sensor elements is relatively simple and the fabricated pressure sensors can be repeatedly used with direct real-time current readout.

2.2.4 Deformable microballoon-based colorimetric method

Embedding a series of microballoons (Banerjee and Mastrangelo 2016) that can expand and contract under external pressure changes into the microchannel can also achieve real-time in-situ pressure measurement (see Fig. 5d). The deformable microballoons (12–15 μm in diameter) consist of 12 μm hollow flexible parylene-C shells with a coating of ultrathin Al_2O_3 diffusion barriers. The spherical microballoons along with their support-stem are fixed in their positions attached to the bottom wall of the channel. The diameter of each microballoon is a function of the pressure difference between the shell exterior pressure and the interior pressure, and the functional relationship can be determined experimentally by a colorimetric method. In the measurement procedure, when the light of a particular wavelength λ is incident on a particle, the intensity of the reflected light is a function of the particle size. The microballoons display a radial pressure sensitivity of 0.44 nm PSI^{-1} within a pressure sensing range of 0–25 PSI (0–172 kPa). The microballoons can be used for mapping the internal pressure drop within microfluidic chips at multiple locations. Furthermore, these microballoons experience nearly spherical symmetry which could make them potential flow-through sensors for the augmentation of particle-based flow characterization methodologies extending today's capabilities of the micro-PIV.

2.2.5 Corner rivulets-bubble-based electrical resistance method

Recently, Tang et al. reported a novel corner rivulets-bubble (CRs-B) pressure sensor device (Tang et al. 2019), as shown in Fig. 5e. The effective volume of the device is only $18 \times 100 \times 580$ μm^3. It uses microfluidics to generate a microbubble spontaneously by sharp capillary forces, which is termed interior corner flow (ICF), which can be seamlessly integrated into the microchannel to perform liquid pressure conversion. The sensor is fabricated into an ultrathin polymer foil (8 μm) including a bumped microchannel (the sensing chamber) and two embedded electrodes. One side of the sensing chamber is closed, and the other side is open with two parallel entrances. When the device is transferred into liquids, due to intermolecular forces, a minute amount (≈ 50 pl) of liquid can "wick" into the sensing chamber through ICF. The inner gas is trapped in the center, forming a long bubble surrounded by liquids all around. The inner liquid–gas–liquid system formed in the sensing chamber constitutes the special pressure-sensitive element, i.e. CRs-B, instead of only bubbles. The two CRs can act as the conductive path when voltage is applied across the bubble. Therefore, liquid pressure can also be characterized by measuring the electrical resistance of the CR. The sensitivity of the sensor within physiological pressure range (0–200 mmHg) is about $0.11\% \cdot L_0$ $mmHg^{-1}$, where L_0 is the initial bubble length.

2.3 Membrane-free side channel methods

Another category of membrane-free method uses a one-end-sealed side channel as the sensing element, which is connected to the microchannel at the location where the pressure needs to be measured. The amount of the displacement of the gas–liquid interface caused by applied pressure can be interpreted through the ideal-gas-law methods, optical methods, and capacitive methods. Recent years have witnessed the emergence of many studies on this technique, as summarized in Table 5.

2.3.1 Ideal-gas-law methods based on displacement of gas–liquid interface

Srivastava et al. utilized the compression of an air segment trapped by a liquid in a one-end-sealed side channel for monitoring the microfluidic backpressure (Srivastava and Burns 2007). The principal component is a microfabricated sealed chamber connected with an inlet channel and no exit. The entrance to the inlet channel is positioned at the location where pressure is to be measured. Pressure measurement is then based on monitoring the movement of a liquid–air interface in the inlet channel as it compresses the trapped air inside the sealed chamber and calculating the pressure using the ideal-gas-law. For gas, a pressure range of 700–100 kPa is obtained with a resolution of 700 Pa. For liquid, the pressure drop in the range from 0 to 4000 Pa was measured with a resolution of 100 Pa. Since this method primarily uses a microfluidic sealed chamber, it does not require additional fabrication steps and may easily be incorporated in several lab-on-a-chip applications for laminar and turbulent flow conditions. While the above-described method works well, care has been taken to ensure that no bubbles are trapped inside the inlet channel, especially while making the external plumbing connections. In addition, evaporation of the trapped liquid plug may lead to erroneous pressure reading and the method may not be applicable to permeable substrates such as PDMS.

Figure 6a shows a rapid-prototyped on-chip vacuum gauge (Kim et al. 2011) which was fabricated with a microchamber containing a constant volume of trapped air. The chip works based on the volumetric expansion and contraction of air trapped in the sealed microchamber. The changes in air volume displace the working liquid into and out of an indicator channel until the reservoir pressure equals the pressure of interest. The displacement of the liquid in the indicator channel provides an optical indicator of the volume change of the reservoir, which can be translated into

Table 5 Membrane-free side channel pressure sensors

References	Sensing elements	Size of devices	Range of measurement	Sensitivity	Response time
An on-chip backpressure-detected sensor (Srivastava and Burns 2007)	A microfabricated sealed chamber connected with a one-end-sealed side channel	8×14 mm^2	700–100 kPa (gas) 0–4 kPa (liquid)	700 Pa (gas) 100 Pa (liquid)	NA
A rapid-prototyped on-chip vacuum gauge (Kim et al. 2011)	A microchamber containing a constant volume of trapped air	NA	0–65 kPa	1.20 mm kPa^{-1} (0–20 kPa)	NA
An easy capillary-based fluid pressure sensor (Shen et al. 2020)	A commonly used capillary with one end sealed and calibrated scales on it	400 µm in diameter and 95 mm in length	101–177 kPa	1 kPa	NA
A micro-nano structure integrated liquid sensor (Yu et al. 2020)	Five trapezoidal metering microchannels and a substrate with MSNP	< 7 cm^2	0.2–20 kPa	167.1 mbar^{-1}	6.3 ± 0.5 s
A fused silica microfluidic device with pressure sensing capability (Zhang et al. 2020)	A capillary and a liquid reservoir	91 mm in diameter	0–200 kPa	0.062 nm kPa^{-1}	NA
An optically readable sensor of backpressure determination (Hoera et al. 2018)	Air-filled side channel with PSP deposited on the surface	NA	0–5 bar	9 mbar	380 ± 25 ms
A non-optical sensor for detecting displacement of gas–liquid interface (Suter et al. 2013)	Two coplanar parallel titanium electrodes	< 6 mm^2	10–200 kPa	−0.834 pF kPa^{-1}	NA
A flexible liquid metal-based capacitive fluid sensor (Zhou et al. 2019)	Capacitor composed of two electrode channels filled with galinstan	NA	20–300 mmHg	0.14 mmHg	< 0.2 ms

the applied pressure using the ideal-gas-law. The dynamic range can be adjusted by changing the trapped air chamber volume. Compared with the method reported by Srivastava and Burns (2007) the preliminary vacuum gauge is capable of measuring sub-atmospheric pressure down to 65 kPa below ambient with a linear sensitivity of 1.20 mm kPa^{-1} for 0–20 kPa below ambient.

However, due to the prior order of microchannel design, the above two methods cannot be used to detect the fluid pressure at one or multiple locations in the existing microchannel. A quick and simple insert capillary-based method (Shen et al. 2020) can roughly solve this problem. The main sensing element is a commonly used capillary (inner diameter of 400 µm and 95 mm in length), with one end sealed and calibrated scales on it. By reading the height (h) of an air–liquid interface, the pressure can be measured directly from a table, which is calculated using the ideal gas law. It is proved that the method can obtain a resolution of 1 kPa within a full-scale range of 101–177 kPa, and the pressure drop of 10 Pa can be obtained in the working range of 70–100 Pa. Furthermore, this method can be used to analyze the nonlinearity of the flow-pressure drop relationship caused by channel deformation.

Recently, Yu et al. presented a micro-nano structure integrated liquid pressure sensor (Yu et al. 2020), which features an ultra-high sensitivity of 16.71 mbar^{-1}, a low-pressure regime of 2 mbar, a trace sample volume of less than 1.3 µl, and a visible display element. This sensor is miniaturized and portable, at less than 7 cm^2. It consists of a primary fluidic microchannel, five trapezoidal metering microchannels, a substrate with hydrophobic microstripe-nanopillar array (MSNP), and a finger pressing gas chamber (Fig. 6b). When the fluidic microenvironment is pressurized, fluids can inject into the metering microchannels from the inlet of the primary microchannel. The air in the metering microchannel is compressed, and according to the ideal-gas-law, the pressure of the fluidic microenvironment can be quantitatively calculated. Finally, the inlet pressure can be measured based on the naked eye reading the amount of MSNP grids where fluids flow through within the five metering microchannels. The adjustable pressure regime is approximately between 2–200 mbar.

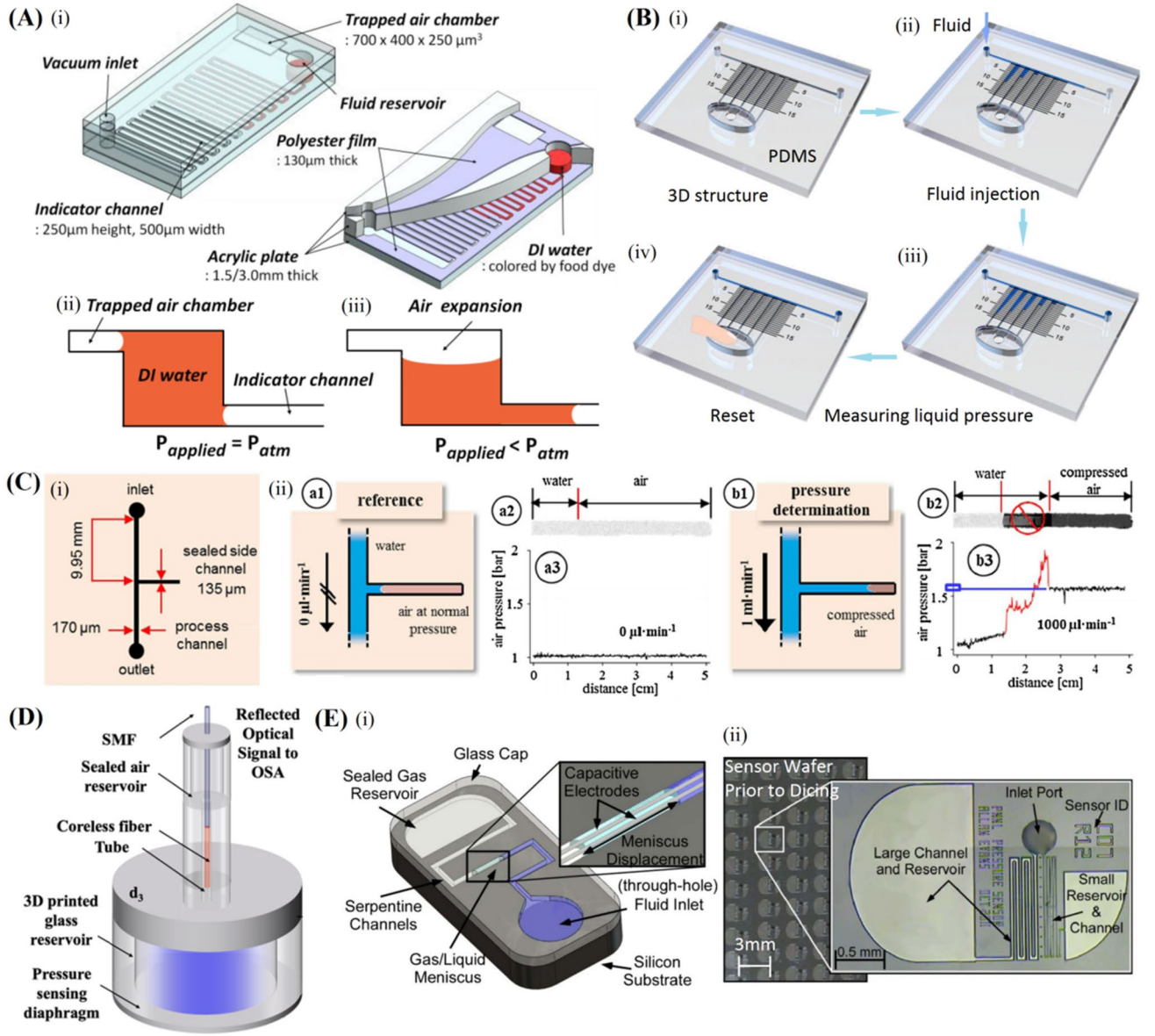

Fig. 6 **a** Illustrations and operation principle of the vacuum gauge for pressure measurement. (i) Top schematic and its 3-D bottom cross-sectional views; (ii) DI water plug under pressure equilibrium. Note the water plug stops at the same position to balance meniscus contact angles; (iii) the water plug slides toward the lower pressure side in proportion to the pressure difference (Kim et al. 2011). **b** Schematic illustration of the liquid pressure sensor. (i) 3D structure; (ii) fluids flow within the sensor; (iii) liquid pressures measured according to the quantity of grids filled by fluids; (iv) reuse of the sensor realized by pressing the gas chamber with a finger. **c** (i) Design structure of an optically readable pressure sensor chip; (ii) determination of spatially resolved back pressure profiles in the side channel (Hoera et al. 2018). **d** Schematic of the microfluidic pressure-sensing device that is interrogated by optical fiber sensing structure (Zhang et al. 2020). **e** Illustrations and operation principle of the capacitive sensor based on displacement of gas–liquid interface. (i) Schematic illustration of the sensor with two parallel sensing electrodes along the length of a serpentine microchannel, which are used to measure capacitance changes as the gas–liquid meniscus is displaced. (ii) Photographs of a portion of the sensor array on a silicon wafer and (inset) a typical two-channel small-footprint pressure sensor with vertical entry port with a large channel width of 40 μm and a small channel width of 10 μm to provide autocalibration of meniscus forces (Suter et al. 2013)

The pressure registration can be instantaneously visualized in-situ without any additional energy source inputs or intricate data acquisition circuits required.

2.3.2 Optical methods based on displacement of gas–liquid interface

While the above method enables an elegant determination of pressures in microchannels, the optical tracing of the liquid–air interface movement as well as the determination of the contact angle is rather challenging and potentially error-prone. For this purpose, Hoera et al. proposed an optically readable approach of backpressure determination using trapped air and an oxygen-sensitive luminescent sensing layer deposited on the air-filled side channel surface (Hoera et al. 2018), as shown in Fig. 6c. The T-shaped side channel with one end closed is led out from the main channel. Due to the increasing flow rate, the backpressure increases, forcing the fluid medium into the sealed side channel and compressing the trapped air inside. This method further uses the PSP technology to sense the displacement of the compressed gas–liquid interface. The employed luminescent molecules are optical chemical sensors that react with oxygen molecules through a quenching mechanism. The local oxygen content can be calculated via the emissive properties of luminescent molecules embedded in highly gas-permeable matrices such as PDMS. By compressing the air in the side channel, the luminous intensity under different air pressures can be obtained and further converted to pressure values after calibration. This sensor allows on-chip pressure sensing with a high sensitivity of up to 9 mbar, working range from 0 to 5 bar, and flow rates in the range between 1 µl min^{-1} and 3 ml min^{-1}, which enables reliable determination of gas pressures, as well as flow rate-induced liquid backpressures at various positions along a channel.

Most of the above-mentioned sensors are carried out in polymer materials (such as PDMS), which benefit from its good optical transparency, biocompatibility, and ease of fabrication by well-developed soft lithography technique. However, PDMS and other polymer-based materials also have some limitations, in particular when considering long-time thermal and chemical stability. Taking advantage of the mechanical stability and great optical transparency of fused silica, Xiao's team fabricated a fused silica microfluidic device with pressure-sensing capability (Zhang et al. 2020). As shown in Fig. 6d, the sensor consists of a capillary and a 3D printed glass reservoir, where the reservoir volume change under pressure manifests liquid level deviation inside the capillary, thus realizing the conversion between small pressure change into large liquid level variation. And an optical fiber-sensing structure is placed inside the capillary, which accurately detects changes in liquid level. The test results show that the pressure sensitivity was 0.062 nm kPa^{-1} at fixed temperature environment. With this all-glass interface, good mechanical robustness, and chemical resistance, this microfluidic device is potentially useful for pressure measurement for biological and chemical applications, especially for specialized microfluidic systems.

2.3.3 Capacitive methods based on displacement of gas–liquid interface

The basic principle is to measure the pressure by detecting the capacitance change caused by the movement of the interface of two immiscible liquids in the side channel. These methods can measure pressure without the need for large optical components or complex electronics, facilitating a large number of integrations.

In an intriguing work, two coplanar parallel titanium electrodes were fabricated along the side microchannel (Fig. 6e) to monitor the capacitance change caused by the displacement of the gas–liquid interface and realized non-optical pressure measurement (Suter et al. 2013). Similarly, this sensor uses the small effective hydraulic diameter of the microchannel to produce the gas–liquid interface (menisci) to trap gas in a sealed chamber. The pressure can be measured by monitoring the capacitance of the electrodes, which are made by micromachining technology and used to measure the displacement of the meniscus that behaves according to the gas laws. The initial sensor devices deliver a sensitivity of -0.834 pF kPa^{-1}, a pressure resolution of 42.5 µm kPa^{-1}, and a small footprint less than 6 mm^2 and can be customized to suit a variety of pressure-sensing applications through mask modifications.

On the contrary, Zhou et al. presented a novel flexible liquid metal-based capacitive fluid pressure sensor, which consists of a middle side detection channel connected to the target working main channel and two electrode channels (Zhou et al. 2019). The two electrode channels, filled with liquid metal (galinstan) as electrodes on both sides of the detection channel with a distance of 384 µm, constitute a capacitor. Any pressure increase in the main channel will cause more working fluid going into the detection channel and the interface of the two fluids going further into the detection channel causing the capacitance change and vice versa. This sensor can achieve a pressure range of 20–300 mmHg with high sensitivity (0.14 mmHg), fast response time (less than 0.2 ms), and high flexible stability. It has been used to detect the pressure fluctuation in a rabbit carotid artery, showing an excellent stability and linear correlation between capacitance and fluid pressure values.

2.4 Other methods

The discovery of the pressure distribution of mixed microflow paths has spawned many novel pressure measurement

methods, which are based on the pressure difference of laminar flows. Combined with the design and calculation of the reference channel, in recent years, researchers have invented many in-situ pressure measurement methods suitable for microflows.

2.4.1 Displacement of a trapped bead in narrow side-channel method

In conjunction with optical capture, Jin et al. measured the additional pressure due to the presence of droplets in two

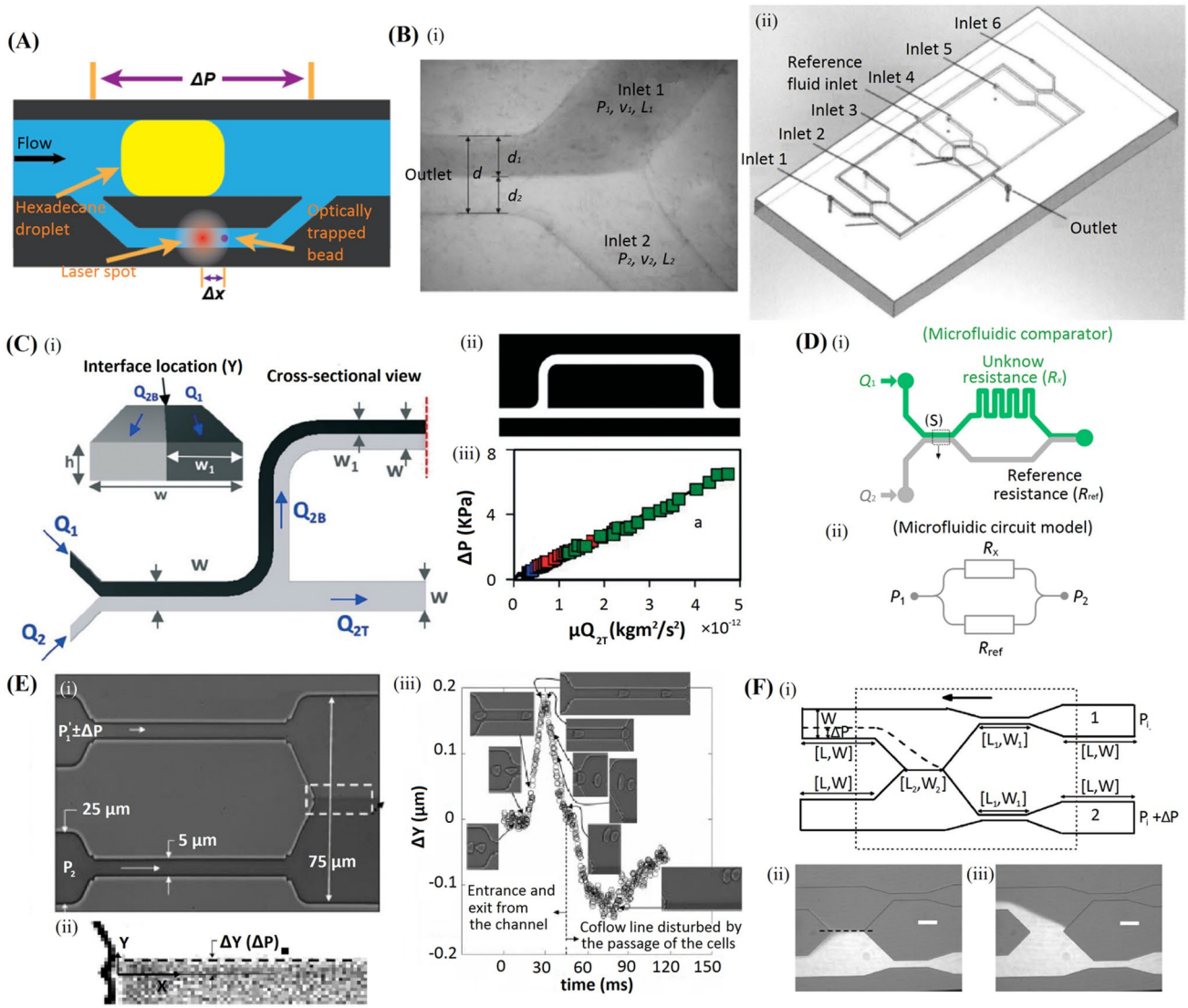

Fig. 7 **a** Schematic diagram of the structure and working principle of the pressure sensor based on the displacement of a trapped bead in a narrow side-channel (Jin et al. 2012). **b** (i) Photograph illustrating the principle of the laminar flow distribution method based on reference flow (Liao et al. 2011); (ii) schematic diagram of a multi-channel pressure measurement chip based on laminar flow distribution (Yang et al. 2012). **c** Basic principle of microfluidic bypass manometry. (i) Schematic of a bypass network labeled with the inlet flow rates of the dyed phase, Q_1, and undyed phase, Q_2. The undyed phase splits between the bypass channel, Q_{2B}, and the test channel, Q_{2T}; (ii) schematic diagram of the microfluidic bypass test chip; (iii) pressure drop versus flow rate relations for microchannels (Suteria et al. 2018). **d** (i) Schematic of the parallel microfluidic circuit consisting of two channels connected in parallel, one of which is colored with a dye; (ii) parallel microfluidic circuit model for comparison region for measure the flow distribution (Choi et al. 2010). **e** Schematic diagram of high-speed microfluidic differential manometer; (i) calibration of the excess pressure drop in the upper channel. When there is no cell flow, the outlet fluid–fluid interface is located in the center of the channel; (ii) image analysis for determination of the variation of the position of the co-flowing line that marks the interface; (iii) variation of the relative position of the interface as a function of time when cells enter the channel (Abkarian et al. 2006). **f** (i) Schematic drawing of the microfluidic comparator. The channel height in the device is 20 μm. The dashed curve represents the interface position resulting in interface displacement of ΔY; (ii) simultaneous bright field and fluorescence images showing the symmetry position (denoted by a dashed line) of the interface at $\Delta P = 0$ and (iii) $\Delta P = 980$ Pa (Vanapalli et al. 2007)

locations of a microchannel (Fig. 7a) (Jin et al. 2012). A shielding structure divides the microchannel into two parallel channels: the main channel is a wider upper channel, and the narrower lower channel is defined as a side-channel. The pressure differentials across the two parallel channels are identical at low Reynolds numbers, which is defined as:

$$Re = \rho U D_h / \mu, \tag{1}$$

where ρ, μ, and U are the fluid density, viscosity, and average velocity in the microchannel, respectively. The D_h is the microchannel hydraulic diameter defined as:

$$D_h = 2WH/(W + H). \tag{2}$$

In the center of the narrower and segmented side-channel, a spherical polystyrene bead is trapped by using an optical tweezer. The fluid drag force exerted on the bead is balanced by the optical restoring forces from the tweezer, giving rise to a slight displacement of the bead from the trap center, and the displacement is related to the pressure difference of the parallel channels. The geometry of the microchannels can be modified to tune the working range of the device over a large span of pressures from several Pascals to several thousand Pascals, amenable to applications in various flow conditions.

2.4.2 Laminar flow distribution methods based on reference flow

A creative hydrodynamic method based on the laminar flow distribution in a Y-shaped confluent structure was proposed by Liao et al. (2011) as shown in Fig. 7bi. The structure consists of two inlets (test flow and reference flow) and a common outlet, where the width of the two fluid flows at the outlet is proportional to its pressure. According to the microscope image processing method, the width ratio of the two liquids at the outlet can be measured, so the pressure of the test channel can be calculated according to the reference channel. Using this method, the same research team further proposed a microfluidic chip for the simultaneous measurement of pressures in multiple channels (Yang et al. 2012), as shown in Fig. 7bii. The six test flow paths converge in the measurement areas to form six groups of laminar flows. The pressure value of each group can be measured according to the occupied width ratio.

2.4.3 Bypass coflowing streams methods

Suteria et al. introduced a microfluidic bypass manometry (MBM) for parallelized measurement of the pressure drop versus flow rate (ΔP–Q) relations (Suteria et al. 2018). As shown in Fig. 7c, it employs co-flowing laminar streams in a microfluidic network that contains a U-shaped by-pass channel as the sensing element analogous to the macroscale U-tube manometer. By recording the fluid–fluid interface in the bypass channel connected to a test geometry, it also shows the capacity to perform parallelized flow resistance measurements.

Two Newtonian fluids of identical viscosity, but one of which is dyed, are injected into the network with known flow rates Q_1 and Q_2. These two co-flowing streams traverse through each loop, with the dyed stream only passing through the bypass channels, whereas the undyed stream splits and flows through the bypass and test geometry. Thus, the ΔP across the test geometry can be obtained from the following two formulas:

$$\Delta P = (Q_1 + Q_{2B}) R_B, \tag{3}$$

$$\frac{Q_{2B}}{Q_1} = f(\alpha, \eta, Y), \tag{4}$$

where R_B is the hydraulic resistance of the bypass that can be calculated from the analytical result for flow through a duct, α is the channel aspect ratio, η is the viscosity ratio of the two fluids, and Y is the interface location between the two fluids. Y is experimentally determined by applying a sigmoid fit to the pixel intensity across the bypass channel. The applicable range of this method for measuring pressure drop is between 100–10,000 Pa, and the accuracy depends on the measurement of the interface location Y, and the measurement error is calculated to be 3%.

Similarly, Choi et al. (2010) presented a parallel microfluidic circuit that directly compares the test channel of an unknown hydraulic resistance with the reference channel with a known resistance (R_{ref}), thereby measuring the unknown resistance without any measurement setup, as shown in Fig. 7d. The microfluidic parallel circuit consists of two channels connected in parallel, one channel of which has an unknown hydraulic resistance (R_x). In the parallel microfluidic circuit, the pressure drop ($\Delta P = P_1 - P_2$) across each channel is the same, and the total volume of fluid through the circuit is the sum of the volumes through all the components by mass conservation. The flow volume through each channel is found by adjusting feeding rates of the two different fluids, one of which is colored with a dye. Therefore, if R_{ref} is known, then R_x can be measured simply by solving a proportional equation in terms of volumetric flow rate and hydraulic resistance. As a means to characterize the newly developed channel segment with predefined standard channels, this method can provide practical design parameters that facilitate design of microfluidic networks (Shaikh et al. 2005). Similarly, Groisman et al. also reported a differential in-situ pressure sensor (Groisman et al. 2003), in which the pressure drop of an unknown liquid stream is measured using an adjacent

liquid stream of known pressure drop with a precision of about 1 Pa.

2.4.4 Displacement of interface in twin channel methods

A typical microfluidic comparator consists of two identical channels that are connected downstream to form the comparison region. To measure the hydrodynamic resistance due to a soft object being present only in the test channel, fluid flow is generated in both the channels with the soft object. When equal driving pressures are imposed at the channel inlets, any increase in hydrodynamic resistance due to the presence of the soft object yields a corresponding displacement of the fluid–fluid interface in the comparison region. For example, Abkarian et al. developed a high-speed microfluidic differential manometer (Fig. 7e) for cellular-scale hydrodynamics with twin channels (Abkarian et al. 2006), i.e. a test channel and an identical control, or "comparator", channel, both of which produce downstream two parallel and adjacent streams of fluid. To maintain a stable interface, the two fluids are miscible, and the liquid flowing through the control channel is dyed to visualize the interface downstream. Hence, the principle of the measurement lies in the use of the second control channel to detect any variation of pressure in the test channel when a cell, or another soft object, is flowing through it. A change in the pressure drop along the channel alters the position of the interface downstream. The measurement of this deflection allows the pressure to be determined after a basic calibration procedure, and consequently, the time-dependent dynamical changes in the pressure drop in the test channel can be monitored. This method is general and can be applied to any dynamic process by changing the hydrodynamic resistance of the test channel relative to the control channel (chemical reactions, changing viscosity, etc.).

In practice, the geometry of the channel will affect the relationship between the excess pressure drop and the measured interface displacement generated by the cells, which is the key to rapid measurement of dynamic variations in hydrodynamic resistance of cells. Vanapalli et al. (2007) optimized the relationship between the pressure drop and measurement interface displacement by changing the geometry of the microchannel with particular focus on enhancing the sensitivity of measuring the hydrodynamic resistance of soft objects. As shown in Fig. 7f, the hydrostatic head at the inlet of the reference channel was increased resulting in a displacement in the interface. Subsequently, then the width of the excess fluid stream in the outlet channel is measured and quantified as the interface displacement ΔY due to the excess pressure head ΔP. This approach of interface displacement measurement in the outlet channel offers greater sensitivity and flexibility by manipulating the aspect ratio of the channel in measurement of hydrodynamic resistance of soft objects. In addition, because of the reduced footprint, this kind of comparator can be placed at any desired location in a complex hydrodynamic circuit.

3 Applications of pressure measurement sensors

As pressure can directly determine the flow rate of fluids, accurate pressure monitoring is an important issue for precise control of cells, particles, droplets, and chemicals. In these applications, hydraulic resistance is an important design parameter that determines whether the device principle works well. Consequently, any microfluidic applications that require a precise knowledge of flow profile and distribution will not be compromised without accurate measurement or calculation of hydraulic resistance. Besides, using the advantages of multidisciplinary research, it can realize the applications of the pressure measurement technology in multiple fields, and its application fields are also expanding, including biology, biomedicine, microfluidic designs and investigation of fluidics physics and so on.

3.1 Biological applications

The interaction of the flow with deformable entities such as polymers (Schroeder et al. 2003) (e.g. DNA), microfoams (Garstecki et al. 2004), cells (Walmsley 2019), and vesicles (Witwer and Wolfram 2021) is a tool to further investigate the details of their mechanical properties and structural features. The flow and shape of any closely fitting soft object are closely related to the properties of the soft object, fluid pressure and viscous stresses acting on the boundary of microflows. The hydrodynamic resistance resulting from this fluid–structure interaction (FSI) is reflected in a dynamical variation of the pressure drop along the microchannel during the flow. In particular, the process of focusing, separating, and transferring a biological sample to a desired location in a pressure-driven microfluidic system is inseparable from real-time pressure monitoring (Chung et al. 2008; Gao et al. 2004; Wheeler et al. 2003). Therefore, precisely monitoring pressure changes is highly desired in biological applications using microfluidic systems.

Generally speaking, non-invasive, non-interference pressure sensors have attracted great interest towards biological applications, such as lead-out side channel method, non-invasive membrane-based method, etc. Moreover, sensors with chemical inertness, biocompatibility, and integration are more suitable for the detection of soft substances, such as silicon carbide membrane (Nguyen et al. 2017). When a single red blood cell enters a 5×5 μm channel, the typical pressure drop varies from tens to hundreds of Pascals. And considering the maximum mechanical stress of soft

materials, the typical pressure range is about 0–3 PSI. The excellent spatiotemporal controllability of flows provided by microfluidics has been intensively exploited to develop various cell culture devices for in vitro cell studies under various controlled cellular-scaled microenvironments (Gu et al. 2004; Zhao et al. 2019). For example, microfluidic devices capable of generating soluble factors and pressure gradients have been developed to provide various mechanical stimulations, including stretch and shear stresses, to enhance the understanding of their roles in regulating a cell's behavior (Douville et al. 2011).

A proper cellular microenvironment for cells or bacteria culture (Liu et al. 2013), which usually requires long-term experiments, can be well maintained by providing media and real-time monitoring of pressure. The concept of electrofluidic circuits for pressure sensing (Wu et al. 2011, 2012) and an equivalent circuit model are combined to design the cell culture channels, which are used to culture human umbilical vein endothelial cells (HUVECs) under various shear stress and hydrostatic pressure combinations (Fig. 8a). In the experiments, HUVECs are cultured in the device with a continuous medium perfusion, which provides the combinatory mechanical stimulations, while the hydrostatic pressures are monitored in real-time to ensure the desired culture conditions. The experimental results demonstrate the importance of real-time pressure monitoring, and how mechanical stimulations affect the HUVECs culture. The device provides a practical platform for an in vitro cell culture under well-controlled and dynamic microenvironments.

In the study of cell behavior, accurate pressure control is essential for studying the mechanical properties of flowing cells inside microchannels and monitoring the occurrence of unexpected events (such as hemolysis). For instance, a high-speed microfluidic differential manometer (Abkarian et al. 2006, 2008) was used to measure the flow pressure drop of a single healthy cells and stiffer cell treated with glutaraldehyde (Fig. 8b). It was found that the pressure drop is enhanced after treatment with glutaraldehyde and hence this approach allows differentiation of cells with different mechanical properties or geometrical features. The hemolytic properties of two types of cells were obtained at the same time. Since organ failure is associated with the rigidity increase of malaria-infected red blood cells (RBCs), this method can be used to examine qualitatively the flow-induced hemolysis of malaria-infected cells, which may provide a simple biomedical tool for clinical hemorheology and pharmaceutical testing.

Many pneumatically adjustable micro-transmission microscope pressure sensors (Orth et al. 2011) with a film thickness of 3 μm and a radius of 15 μm are arrayed to monitor the pressure drop of the chicken RBCs flowing through the constrictions under pressure driven flow. When an RBC occupies the constriction, it increases the hydraulic resistance across the constriction leading to an increase in the pressure drop. Therefore, a typical pressure curve of chicken RBCs under mechanical compression in a microchannel was obtained to achieve high-throughput cell mechanics measurement (Fig. 8c). This technique compares the relative magnitude in pressure dips that occur on a time scale of tens of milliseconds. It has important significance for in vitro microcirculation diagnostics.

3.2 Biomedical devices

Biomedical devices usually require the detection range of the sensor to cover the physiologically relevant blood pressure range found in humans (0–142.5 mmHg), and require a faster response time (less than 0.5 s). Different application backgrounds need to cooperate with sensors of different structures, and the following fine areas are mainly involved in the field of microfluidics:

3.2.1 Organs-on-chips devices

Pressure also plays an important role in medical systems. Microfluidic cell culture devices, namely organs-on-chips, simulating the activities, mechanics, and physiological responses of entire organs and organ systems have recently been developed (Park et al. 2019). These microfluidic devices, mimicking the structural tissue arrangements of organs, such as kidneys, lungs, and livers, are capable of precisely controlling dynamic flows and pressures on the micrometer scale, which makes the reconstitution of more physiological meaningful cellular microenvironments in vitro possible (Hu et al. 2019; Huh et al. 2010; Nakao et al. 2011). Studying cells in microenvironments similar to those in vivo permits a better understanding of diverse biological processes.

Chen et al. (2017) integrated an on-chip capillary-assisted pressure sensor (Srivastava and Burns 2007) with microfluidic circulation system to closely mimic human systemic circulation in vitro (Fig. 8d). The sensor covered the physiologically relevant blood pressure range found in humans (0–142.5 mmHg) and could respond to 0.2 s actuation time. With the aid of the sensor, the pressure inside the device could be adjusted to the desired range. Research also found that HUVECs were cultured on-chip and cells can respond to mechanical forces generated by arterial-like flow patterns. This microfluidic circulation system with in situ pressure sensors can be further applied in a variety of research fields, including blood circulation physiology research, drug screening, and disease modeling.

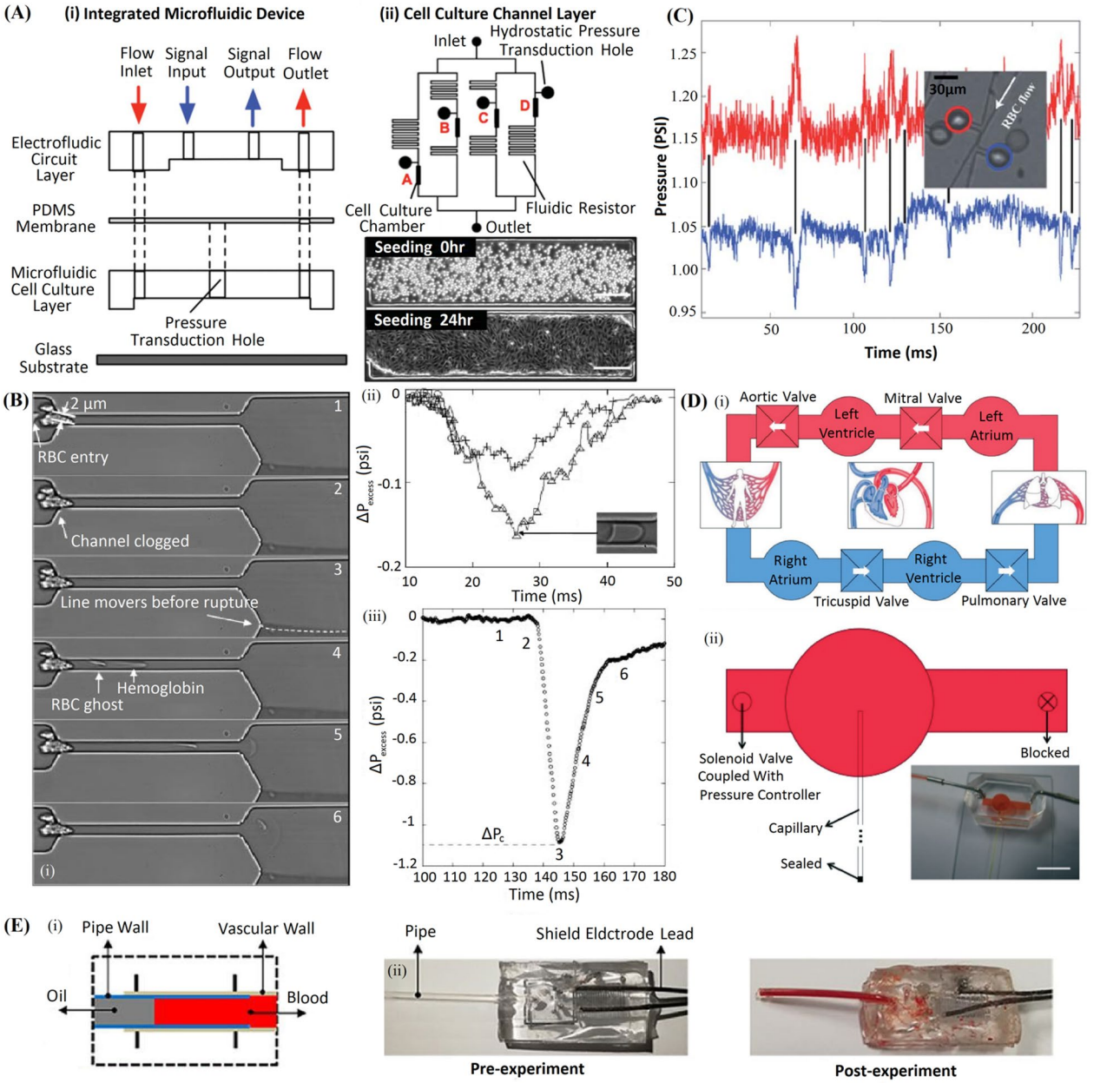

Fig. 8 **a** Schematic representations of the microfluidic cell culture device with embedded electrofluidic circuit pressure sensors. (i) The schematic illustration of the device with a PDMS membrane is sandwiched by two PDMS layers: an electrofluidic circuit layer and a microfluidic cell culture layer, and a glass substrate; (ii) the layout of the microfluidic cell culture layer and its equivalent fluidic circuit model; (iii) images of HUVECs seeded and cultured for 24 h inside a microfluidic device (Liu et al. 2013). **b** Measuring the mechanical properties of flowing cells using the high-speed microfluidic differential manometer. (i) Hemolysis of an RBC passing through a narrow constriction; (ii) pressure drop versus time for different conditions characterizing the state of the RBCs; the driving pressure is 5 PSI, healthy RBC (+), RBCs treated with 0.001% glutaraldehyde (open symbols); (iii) pressure drop versus time for RBC hemolysis (Abkarian et al. 2006). **c** Pressure traces of two pneumatically adjustable micro-transmission microscope sensors on either end of a 5-mm constriction. Inset: micrograph of the device, obtained with a 4× objective lens (Orth et al. 2011). **d** (i) Schematic showing the concept of the microfluidic circulatory system; (ii) schematic showing the experimental set-up of the sensor characterization. The inset shows the photograph of the device filled with red ink solution and integrated with a capillary-assisted pressure sensor (Chen et al. 2017). **e** Experimental process of the microfluidic blood pressure sensor. (i) Implantation position of the blood pressure sensor; (ii) sensor chip before and after the experiment (Zhou et al. 2019)

3.2.2 Implantable monitoring devices

Pressure sensors can also be used for implantable pressure monitoring, such as intracranial pressure sensor (Chesnut et al. 2012), in bladder pressure sensors (Majerus et al. 2012) and in cardiovascular pressure sensors (Chow et al. 2010). These sensors are integrated into an intraocular lens, stents, or catheters and perform 24 h monitoring of various clinical parameters. For example, Zhou et al. successfully implanted the liquid metal-based capacitive pressure sensor (Zhou et al. 2019) into a living body and detected the pressure fluctuation in a rabbit carotid artery (Fig. 8e). After injecting norepinephrine into its ear vein, the capacitive pressure sensor responded quickly and obviously.

In addition, the above-mentioned metering method requires a significant volume of blood to fill a liquid column, while the liquid pressure sensor (LPS) (Yu et al. 2020) provides a promising alternative, due to its high sensitivity and small sample volume requirement. The LPS is connected to the proximal cerebral end of the right external jugular vein of the rat, and the rats having a low blood volume could be diagnosed according to the quantity of grids filled by the bloods. The sensitivity of the LPS for blood was found to be 16.71 $mbar^{-1}$. The LPS is demonstrated to function well, for common liquids within an ultra-wide surface tension range, enabling its application for detecting the central venous pressures (CVP), and diagnosing the morbidity of hypertension, hypotension and arterial thrombosis.

3.2.3 Wearable monitoring devices

Pressure sensing elements based on microfluidic technology have gradually been widely used in wearable devices due to their good operational flexibility and high sensitivity. Different from the fluid monitoring in the microchannel, the pressure of the wearable device comes from the outside, such as pulse, vocalization, as well as limb movements, while the structure and principle of the two sensors have many similarities. Conventional rigid pressure sensors are unsuitable for the development of wearable electronics due to their fragility and low flexibility arising from their rigid material components. However, thin-film-based flexible sensors can usually achieve flexible pressure monitoring in such applications. Using optical method based on displacement of gas–liquid interface could achieve the detection of intraocular pressure (IOP) sensors, which can be used for the diagnosis and treatment of glaucoma (An et al. 2019; Araci et al. 2014; Chitnis et al. 2013; Varel et al. 2014).

In recent years, with the extensive research of conductive materials, diaphragm-based capacitive/resistive pressure sensors have received more attention in wearable applications. For example, conductive materials such as liquid metal (Gao et al. 2017) and carbon nanomaterials (Toan et al. 2018) are used as sensing elements. Among them, the microfluidic tactile diaphragm sensor based on embedded Galinstan microchannels is used in a PDMS wristband with an embedded, liquid–metal-based pressure sensor capable of real-time pulse monitoring and a PDMS glove with multiple embedded sensors to provide comprehensive tactile feedback of a human hand when touching or holding objects are demonstrated. The one-side-electrode-type capacitive flexible pressure sensor composed of conductive material and PDMS flexible film converts the pressure signal into an electrical signal (Nawi et al. 2015), which can realize tactile touch monitoring and a fast response time of 0.12 s. A flexible pressure sensor based on conductive porous PDMS foam embedded in graphene (Wu and Li 2020), whose response time is 20 ms, demonstrates accurate and real-time monitoring of athletes' tiny physiological signals (including pulse and electrocardiograph signals), vocalization and facial emotions, as well as violent joint and limb movements.

3.3 Microfluidic designs and investigation of fluidics physics

3.3.1 Design of lab-on-a-chip devices

Many of lab-on-a-chip devices can precisely transport fluids along with a channel network with complex patterns. Therefore, it is important to accurately characterize and measure the hydraulic resistance of each channel segment and determine whether the device principle works well. Generally speaking, the working pressure of microfluidic lab-on-chip equipment is usually in the range of several kPa, except for some high-pressure microfluidic controls up to 30 MPa (Hasselbrink et al. 2002). Therefore, most of the sensors mentioned above are applicable in principle. However, the best choice is to directly measure the pressure in situ along with the design of the chip structure, such as non-invasive membrane-free side channel methods, Laminar flow distribution methods, bypass coflowing streams methods, and displacement of interface in twin channels methods.

For example, Groisman et al. demonstrated two microscale nonlinear fluidic devices that can operate at arbitrarily low Re, i.e. a flux stabilizer, which is analogous to an electronic constant-current source (Fig. 9ai), and a bistable flip-flop, which is analogous to a digital flip-flop memory (Fig. 9aii) (Groisman et al. 2003). Among them, the auxiliary channel (b) and the comparator area (c) in the flux stabilizer realize the in-situ monitoring of the pressure by the Y-shaped differential method. The bistable flip-flop uses the crossroad and the compensation channel to perform in-situ pressure measurement. The device combines the non-Newtonian rheological characteristics of viscoelastic polymer solution on the basis of the design of the microfluidic chip to realize the design of an integrated microfluidic

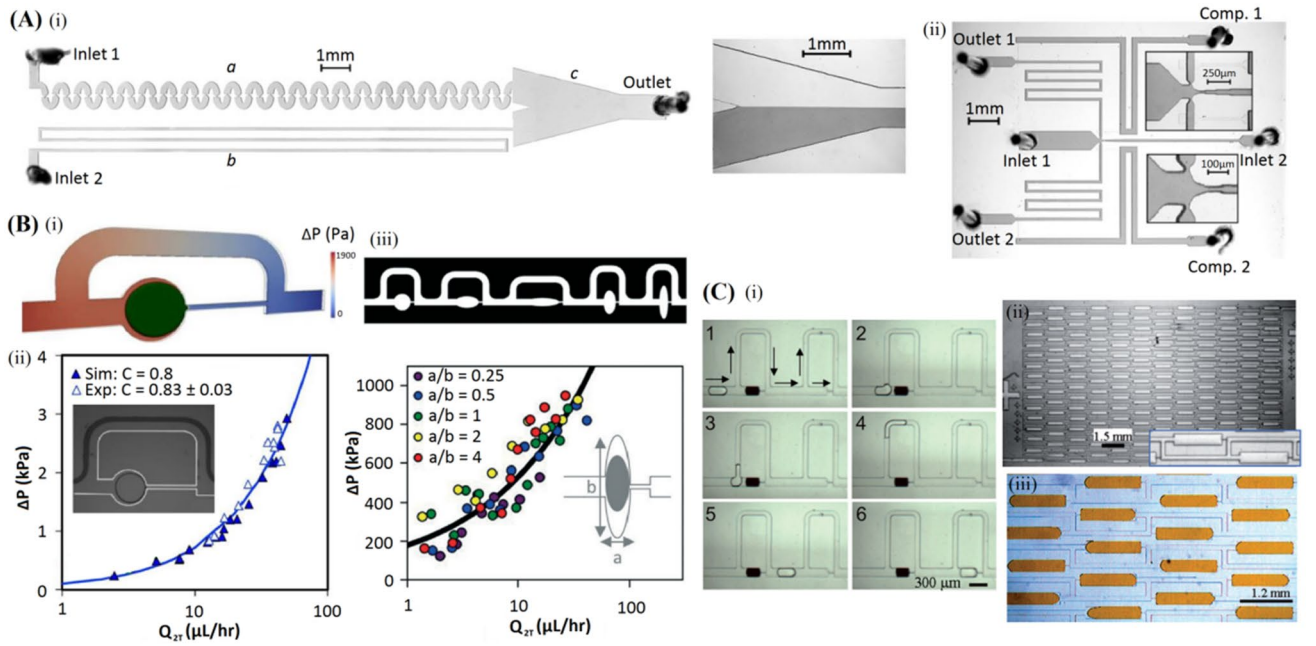

Fig. 9 **a** (i) An image of the nonlinear resistor. Channel a is the functional nonlinear device, whereas rectilinear auxiliary channel b, and the comparator region, c, serve to make a differential in situ measurement; (ii) a snapshot of a flip-flop with modulation of pressure between the metastable states. The pressure is measured locally, near the crossroad exits, with the aid of two auxiliary inlets, components 1 and 2. They are connected to the outlet channels by high-resistance narrow ducts, seen in the insets and do not disturb the main flow (Groisman et al. 2003). **b** Measurement of flow resistance of oil droplets trapped in circular disk-shaped cavities. (i) Image from simulation showing the trapped drop and the pressure drop distribution in the midplane of the channel; (ii) pressure drop versus flow rate results from simulations and experiments; pressure drop versus flow rate data for trapped oil drops in (iii) triangular traps with different aspect ratios, *a*/*b*. The inset shows a representative cavity shape with a trapped droplet (Suteria et al. 2018). **c** (i) Sequential of droplets storage based on hydrodynamic resistance; (ii) high-density storage chip of a symmetrical design. Each storage area is 200 μm wide and the volume is 25 nl; (iii) picture of storage area filled with dyed water and channels filled with oil (Boukellal et al. 2009)

device controlling system. By changing the position of the gas–liquid interface of the compressed capture gas in the microfluidic chip, the rupture pressure of the microfluidic trap is successfully characterized (Dal Dosso et al. 2019). The results show that the presented hydrophobic valve shows both superhydrophobic properties (contact angle up to 155°) and high resistance to liquid pressure (up to 9 kPa), while utter fabrication simplicity.

The transport and manipulation of emulsions, especially microfluidic droplets, are at the heart of many microfluidic devices. The extra pressure caused by droplets is often a key factor in their design and functionality. For example, some "digital" microfluidic devices use droplets or bubbles as logic signals and rely heavily on the extra pressure that they provide to control logic gates and switches (Cheow et al. 2007; Prakash and Gershenfeld 2007). As a result, the successful design and operation of droplet logic is based upon accurate knowledge of the pressure differentials across droplets of different sizes and in various flow conditions. Furthermore, the size of bubbles in a gas–liquid multiphase flow is highly dependent on the pressure in the gas flow (Günther and Jensenb 2006). Some technologies use bubbles or droplets to disturb the laminar flow patterns that occur at low Reynolds numbers and thereby accelerate micromixing processes in the continuous phase (Garstecki et al. 2006). The altered pressure distribution resulting from bubbles has a significant impact on the velocity and residence time of the other bubbles, as well as the continuous phase in the mixing units, and can, therefore, affect the quality and efficiency of mixing.

Drops are considered as "micro-reactors", as each drop can be the site of an independent experiment in microfluidics. Droplet-based biochemical assays and microparticle syntheses present a considerable challenge for device miniaturization (Jung et al. 2016), since the large actuating pressure necessary to sustain the flow of an ensemble of droplets in high-throughput experiments is demanding for the design of micropumps that can be integrated on the chip (Laser and Santiago 2004). Membrane-based devices are in general not appropriate for measuring pressure differentials due to droplets, since deformation of the membrane alters the simple rectangular geometry of the channel cross-section, rendering it difficult to interpret and model the results for droplets. Therefore, most researches on monitoring the pressure of

droplets tend to choose chip structures with pressure measurement functions. In recent years, many studies have tested the pressure drop of droplets flowing through different forms of microchannels in different ways. For instance, Jin et al. employed the method of displacement of trapped bead in narrower side channel (Jin et al. 2012) to measure the extra pressure caused by water droplets in hexadecane at higher pressures and larger capillary numbers (Ca), defined as:

$$Ca = \mu V/\sigma, \tag{5}$$

where μ is the viscosity of liquid water, V is the mean velocity of liquid water, and σ is the surface tension of the fluid/fluid interface. They also studied the dependence of extra pressure on droplet sizes. The results show that the competition between viscous dissipation and capillary forces of different droplets affect the pressure value. Such a competition gives rise to the observed non-monotonic relation between extra pressure and droplet length.

To study the interaction between the droplet and the trapping microcavity wall, Bithi et al. recorded the ΔP–Q data for oil droplets trapped in circular-disk shaped microcavities using the microfluidic bypass manometry (MBM) method (Bithi et al. 2017; Suteria et al. 2018), and compared the results with 3D volume-of-fluid (VOF) computational fluid dynamics (CFD) simulations (Fig. 9b). They further studied the influence of cavity shape on the flow resistance of trapped droplets. The results show that the ΔP–Q relation is nonlinear and the flow resistance of droplets is sensitive to the boundary shape of the channel, that is, the MBM method enabled rapid identification of different cavity geometries. At high flow rates, the drop resistance depends on the cavity geometry and is higher in a triangular prism compared to a circular disk. Further, since the resistance of the trapped droplet is related to the capillary number, the bistable behavior of droplet flow resistance can be achieved under different capillary numbers. Taken above together, the results indicate that a trapped drop at a bifurcation can act as a nonlinear resistor and could be potentially used as a soft switch to control droplet trajectories in microfluidic devices.

Boukellal et al. (2009) employed a single microfluidic device with a function of monitoring pressure drop and described the methods for the passive storage of aqueous drops in a continuous stream of oil without any external control but hydrodynamic flow. This device is based on capillary action and changes of hydrodynamic resistances induced by the presence of drops introduced into the channel network. As shown in Fig. 9c, the device contains a droplet storage area and a narrow channel area, and it uses the hydrodynamic resistance of the narrow channel to control the droplets into different storage areas. This device is simple to manufacture, robust under operation, and drops never come into contact with each other, making it unnecessary to stabilize drops against coalescence. Furthermore, this microfluidic design also has the advantage to allow drop extraction from the storage wells by simply reversing the direction of flow in the device.

3.3.2 Deformation of elastic microchannels

Each kind of microfluidic device used for mixing, separation, analysis, sensing, and chemical reaction, is ruled by the fluid flow dynamics. However, the internal pressures of the microchannels are usually monitored by traditional commercial pressure sensors (Cheung et al. 2012; Raj and Sen 2016; Raj et al. 2017, 2018a, b, 2019). Limited by these pressure sensors, the cost, experimental accuracy, and convenience of many studies related to fluid mechanics cannot be well resolved. Instead, in situ monitoring of the internal pressure in microfluidic devices using high-precision, non-invasive methods can provide more accurate information on the site-specific pressure.

For pressure-driven liquid flows in microfluidic devices made of elastomers such as PDMS, deformation of the microchannel by the internal pressure is inevitable, which results in disturbance of the flows within the microchannel (Raj et al. 2018a, b). Further, the pressure drop induced by channel deformation also causes pressure difference between the pressure applied to the apparatus and the actual pressure inside the microchannel. This pressure difference interferes with the precise analysis of pressure-related flow (Gervais et al. 2006; Martínez-Calvo et al. 2020; Yalikun et al. 2020).

In recent years, measuring fluorescence intensity has been a common approach for pressure sensing. Fluorescence microscopy provides a simple and cost effective alternative to confocal microscopy for measuring the deformation of PDMS microchannels. This technique can provide accurate results matching the current theoretical models. Hardy et al. (2009) visualized the deformation of pressurized PDMS microchannels by filling them up with a fluorescent dye. The relationship between wall thickness and channel deformation has been investigated. Pressure and fluorescence intensity were measured at five positions along the length of the channel. As a result, a linear relationship between pressure and microchannel deformation is measured (Fig. 10a). Additionally, the pressure drop through flexible-walled microchannels was measured at up to 35% less than the pressure drop in identically sized rigid-walled channels. That is, the pressure drop in the thin-walled channel was lower than the pressure drop in the thick-walled channel. Similarly, Ozsun et al. (2013) also estimated the pressure distribution in a deformable microchannel using a fluorescent dye and optical interferometry.

Choi and Shim (2019) introduced five deformable colloidal crystal membrane pressure sensing units into a 10 mm-long microchannel at 2 mm intervals (Fig. 10b), and

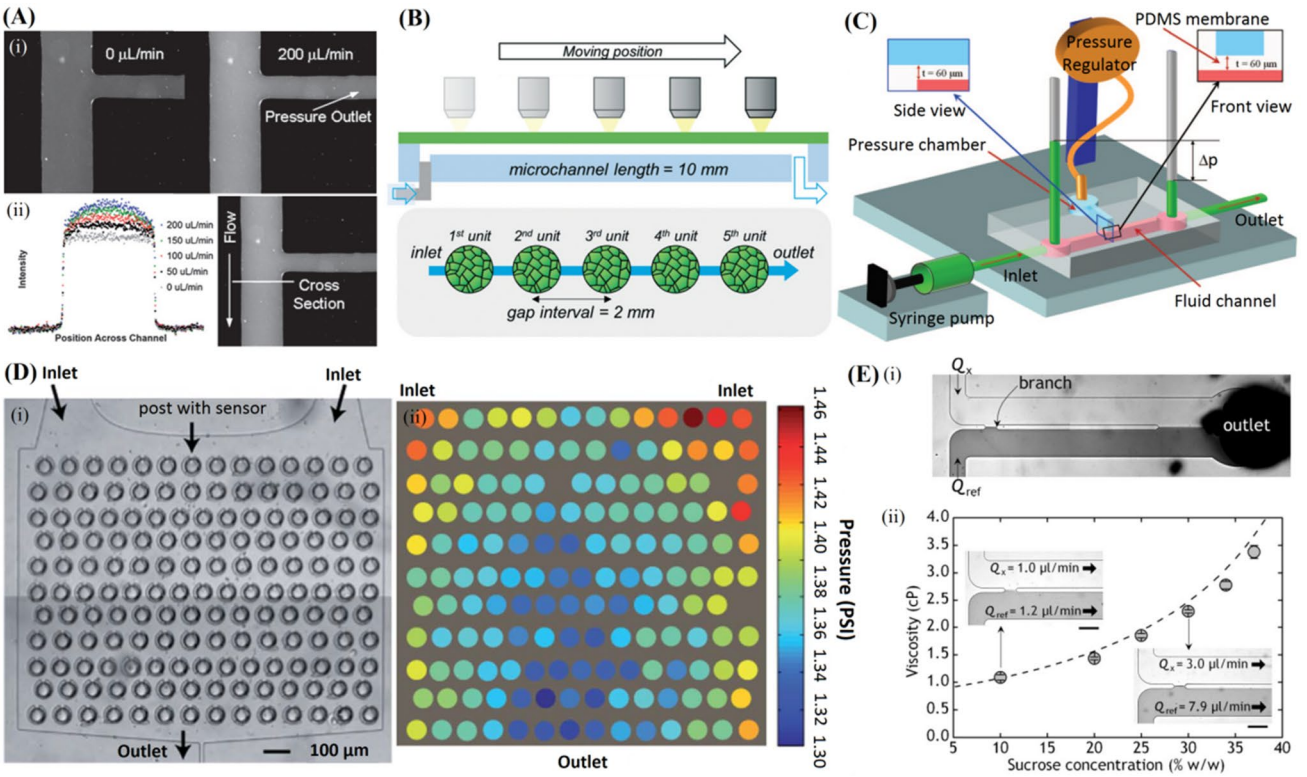

Fig. 10 **a** (i) Channel deformation due to high flow rates, which can be seen in the increased fluorescence intensity of the images of the channel section. (ii) A plot of fluorescence intensity measured across the channel cross-section. Higher flow rates induce greater intensity due to channel deformation (Hardy et al. 2009). **b** Schematics of the experimental set-up for site-specific sensing of pressure in microchannel. Five circular deformable colloidal crystal membrane sensing units with diameter of 300 μm were placed at 2-mm intervals (Choi and Shim 2019). **c** Illustration of the experimental setup, indicating the inlet and outlet ports, methods of flow control and pressure measurement, and the short region over which the channel is deformed using an external pressure applied tangent to the main fluid channel (Chakraborty et al. 2012). **d** (i) Multiple pneumatically tunable microlenses manufactured in PDMS to simulate porous media structures while performing pressure measurements; (ii) the local fluid pressure under steady flow is color-coded from red at high pressure to blue at low pressure (Orth et al. 2011). **e** (i) Optical micrograph of the microfluidic rheometer showing a parallel branch channels design, which is composed of two 700 μm-width parallel channels with a small branch channel connecting them; (ii) measured viscosity as a function of sucrose concentration. The inset shows the balance of the interface positions of two fluids with different viscosities in the branch channels (Choi and Park 2010)

they also observed the pressure gradient along the flexible channel. On the other hand, freestanding colloidal crystal membranes were engineered to monitor the change of the internal pressure at a fixed position with time-varying flow. The time-variant internal pressure in the microchannel was measured while different flow rates were applied using an infusion pump. The results show that the internal pressure increases slowly and settles approximately 1000 s after operation. The internal equilibrium pressure in the binary flows increases slightly as the interval increases, although the average flow rate programmed for the syringe pump is the same. The results reveal the mismatches between the applied pressure and actual pressure, which is due to the hydrodynamic capacitance in the microfluidic system.

The behaviors of deformable microchannels under a pressure-driven flow have also been studied by researchers, and the corresponding flow physics have been modeled. For example, aiming at the complex fluid–structure interaction that arises between a flowing fluid and a deformable wall, Chakraborty et al. (2012) fabricated a flow-through microchannel structure with PDMS, as shown in Fig. 10c. They introduced a pressure microchamber at both ends of the microchannel and measured the pressure within microchamber using the ideal-gas-law method based on sensing the gas–liquid interface displacement by using an inserted capillary. The measured results of thin layer deformation and pressure drop were compared with their proposed two and 3D computational models, which numerically solve the coupled set of equations governing both the thin layer elasticity and fluid. It has shown an excellent agreement between the predictions of the deformed thin layer shape under an externally applied air pressure. Moreover, the two-dimensional model reasonably approximates the 3D

model when the width of the thin layer is beyond roughly twice the length of the thin layer.

3.3.3 Rheology of complex fluids

The seepage of fluid in porous media is the macroscopic manifestation of its flow in countless micron-sized pore throats. Evaluation of pressure perturbations due to droplets and other emulsions in underground pores is key to enhanced oil recovery, (Cobos et al. 2009) and microfluidic devices provide an ideal platform to mimic such porous environments and measure this pressure in laboratories. Orth et al. (2011) obtained two-dimensional pressure maps by setting an array of pneumatically adjustable micro transmission microscope, i.e. posts with sensors (Fig. 10d), which can both enable pressure measurements and serve to add an element of disorder to the flow environment to mimic a porous medium. The design of this microfluidic device is similar to the environment encountered in oil-saturated rock, which is conducive to the study of fluid flow behavior in complex fluid environments.

Using the parallel branch channels to measure the pressure drop, Choi and Park (2010) demonstrated a new kind of rheometer (Fig. 10ei), which balances the position of the interface between a sample and reference fluid with a common pressure drop, thereby enabling a simple and accurate measurement of fluid viscosity and eliminating the complicated theoretical calculations. The microfluidic rheometer is first characterized with sucrose solutions of known viscosity for calibration. The result (Fig. 10eii) shows a concentration-dependent increase in the viscosity of the sucrose solution. Then by measuring minute changes in a rheological property of bovine serum albumin (BSA), the rheometer demonstrates a robust ability in practical applications.

3.3.4 Pulsating flow

The study of pulsating flow is of great significance in the fields of bionic vascular flow. However, factors such as pressure fluctuations, velocity pulsations, non-Newtonian characteristics, and elastic materials make the flow mechanism complicated. Raj et al. (2019) used a commercial pressure sensor to build a pressure sensing system platform and compared the ideal Womersley solution with the other three cases (flexible channel, non-Newtonian fluid, and high-frequency pulsations) to delineate the effects of the deformability and the non-Newtonian fluid flow on the averaged velocity profile in the channel for different phase angles in a pulsating cycle. The local hydrodynamics within the microchannel is found to be more significantly affected by pressure waveform rather than the actual wall deformation and the velocity profile.

In short, the studies on applications of new microchannel pressure measurement methods to achieve real-time and accurate pressure measurement are important and have broad application prospects in fluid mechanics-related researches.

4 Conclusions and perspectives

This review aims to present a deeper fundamental understanding of the recent progress of the mechanisms and applications of pressure measurement methods in microchannels. Micro-PIV can be used as the golden method for the fluid flow velocity vector field, and searching for its complementary pressure field measurement method has always been a popular focus of interest among researchers. However, channel sizes in the microfluidic applications are in the range of 1–1000 μm, which is too small to use in commercial sensors. And physical phenomena at microscales can be quite different compared with those at macroscales because of the small characteristic size. At microscales, issues such as viscous effect, gas compressibility effect, slip boundary condition, and wall wettability and deformation become dominants. Pressure sensing methods or sensors based on microfluidic could be compatible with the microchannels size. Whether it is a traditional film-based multiple methods, a novel type of membrane-free sensing method, or a detection method that utilizes the hydraulic properties of the channel structure, pressure detection can be achieved in the microchannel on a specific occasion. Although the mentioned methods have some clear advantages, there still exist some practical challenges in specific applications which need to be solved in the future.

The optimization of the sensor structure should be the first thing to be considered. In fact, it is difficult for one method to be always superior to others for all applications. For example, although membrane-based optical methods are widely studied and more practical, they often require a sophisticated readout setup (e.g. interferometry, confocal microscopy) and expensive optical equipment with complicated analysis, such as lasers and position- or intensity-sensitive detectors to detect membrane displacement. Membrane-based capacitive and resistive sensors are promising due to the high sensitivity and high spatial resolution of the tactile sensors of an array-type. However, complicated fabrication processes, such as metal deposition and etching, are required; thus, this sensor type is unsuitable for integration in microfluidic systems. Furthermore, the sensor can possibly be damaged due to a large deflection or unexpected impact as this sensor type generally uses mechanically brittle materials, e.g. silicon, carbon fiber, and conductive polymer. For another example, the membrane-free side channel methods does not require external large-scale instruments to obtain images

and the complicated analysis steps to estimate the pressure, but this air trapped method is not suitable for air permeable substrates such as PDMS; it is not possible to ensure that there are no air bubbles in the indicating channel during the measurement (especially when connecting external pipes). In addition, evaporation of the liquid column trapped in the channel may cause incorrect pressure measurement. Using glass channels instead reduces flexibility and increases costs. Moreover, this method also needs modification in the shape of the microchannel geometry that brings extra cost and efforts in the measurement process. Methods that require little or no modifications to the microchannel geometry may introduce more flexibility for the microfluidics. Although some of the current methods could address some of those issues, a pressure measurement technique, which would address all of the aforementioned issues, would be crucial for the further development of the microfluidics and for the fundamental understanding of the fluid flow at microscales.

Due to the advantages of microfluidics being able to intersect with multidisciplines, pressure measurement technology in microchannels has been expanding in the abovementioned emerging application fields, including biology, biomedicine, microfluidic design, and fluid physics research. But most of the miniature pressure sensors or structures presented in this review are still in the proof-of-concept stage. Few of them have verified its widespread effectiveness in atypical microchannels. For example, While optical interface tracking is proposed to measure pressure fluctuations in multiphase flows and detect the pressure differential across single droplets, high-throughput measurements might still be difficult as the geometry of these devices prohibits continuous measurement of single droplets at a high speed since the droplets inevitably disturb the fluid–fluid interface. And generally speaking, the calibration and verification of pressure measurement technology for microfluidic applications require relatively complicated procedures, which undoubtedly increases the barriers to application conversion. Therefore, there still need to integrate multiple methods to achieve simpler integration process, more convenient calibration procedure, and lower design cost to provide high accuracy and rapid response time, thereby reducing the gap between theoretical equipment and applications.

In sum, future studies on micro-scale pressure measurement technology should be focused on improving all aspects, including but not limited to the width and specificity of the pressure measurement range, the convenience of device integration and operation, and the accuracy, immediacy, and non-invasiveness of pressure monitoring. Future micro-scale pressure sensors should be able to real-time detect pressure in a fully automated, more cost-effective, and more compact manner. Therefore, pressure measurement techniques at microscales and these different applications will continue to be challenging and an open-ended research topic for future studies.

Acknowledgements This work is supported by the National Natural Science Foundation of China (11572013 and 11872083) and Beijing Municipal Natural Science Foundation (7152012).

Declarations

Conflict of interest The authors declare that they have no conflict of interest.

References

Abe S, Okamoto K, Madarame H (2004) The development of PIV-PSP hybrid system using pressure sensitive particles. Meas Sci Technol 15:1153–1157

Abkarian M, Faivre M, Horton R, Smistrup K, Best-Popescu CA, Stone HA (2008) Cellular-scale hydrodynamics. Biomed Mater 3:34011

Abkarian M, Faivre M, Stone HA (2006) High-speed microfluidic differential manometer for cellular-scale hydrodynamics. Proc Natl Acad Sci USA 103:538–542

An H, Chen L, Liu X, Zhao B, Zhang H, Wu Z (2019) Microfluidic contact lenses for unpowered, continuous and non-invasive intraocular pressure monitoring. Sens Actuators A Phys 295:177–187

Araci IE, Su B, Quake SR, Mandel Y (2014) An implantable microfluidic device for self-monitoring of intraocular pressure. Nat Med 20:1074–1078

Banerjee N, Mastrangelo CH (2016) Microballoon pressure sensors for particle imaging manometry in liquid and gaseous media. Analyst 141:1413–1420

Bithi SS, Nekouei M, Vanapalli SA (2017) Bistability in the hydrodynamic resistance of a drop trapped at a microcavity junction. Microfluid Nanofluid 21:164

Bogaerts W, De Heyn P, Van Vaerenbergh T, De Vos K (2012) Silicon microring resonators. Laser Photonics Rev 6:47–73

Boukellal H, Selimovic S, Jia Y, Cristobalb G, Fraden S (2009) Simple, robust storage of drops and fluids in a microfluidic device. Lab Chip 9:331–338

Chakraborty D, Prakash JR, Friend J, Yeo L (2012) Fluid-structure interaction in deformable microchannels. Phys Fluids 24:102002

Chaudhury AR, Pantazis AK, Chronis N (2016) An image contrast-based pressure sensor. Sens Actuators A Phys 245:63–67

Chen Y, Chan HN, Michael SA, Shen Y, Chen Y, Tian Q, Huang L, Wu H (2017) A microfluidic circulatory system integrated with capillary-assisted pressure sensors. Lab Chip 17:653–662

Cheow LF, Yobas L, Kwong DL (2007) Digital microfluidics: droplet based logic gates. Appl Phys Lett 90:54107

Chesnut RM, Temkin N, Carney N, Dikmen S, Rondina C, Videtta W, Petroni G, Lujan S, Pridgeon J, Barber J, Machamer J, Chaddock K, Celix JM, Cherner M, Hendrix T (2012) A trial of intracranial-pressure monitoring in traumatic brain injury. N Engl J Med 367:2471–2481

Cheung P, Toda-Peters K, Shen AQ (2012) In situ pressure measurement within deformable rectangular polydimethylsiloxane microfluidic devices. Biomicrofluidics 6:26501

Chitnis G, Maleki T, Samuels B, Cantor LB, Ziaie B (2013) A minimally invasive implantable wireless pressure sensor for continuous IOP monitoring. IEEE Trans Biomed Eng 60:250–256

Cho ST, Najafi K, Lowman CE, Wise KD (1992) An ultrasensitive silicon pressure-based microflow sensor. IEEE Trans Electron Dev 39:825–835

Choi S, Lee MG, Park JK (2010) Microfluidic parallel circuit for measurement of hydraulic resistance. Biomicrofluidics 4:34110

Choi S, Park JK (2010) Microfluidic rheometer for characterization of protein unfolding and aggregation in microflows. Small 6:1306–1310

Choi JH, Shim TS (2019) Real-time pressure monitoring system for microfluidic devices using deformable colloidal crystal membrane. Lab Chip 19:3954–3961

Chow EY, Chlebowski AL, Chakraborty S, Chappell WJ, Irazoqui PP (2010) Fully wireless implantable cardiovascular pressure monitor integrated with a medical stent. IEEE Trans Biomed Eng 57:1487–1496

Chung K, Crane MM, Lu H (2008) Automated on-chip rapid microscopy, phenotyping and sorting of *C. elegans*. Nat Methods 5:637–643

Chung K, Lee H, Lu H (2009) Multiplex pressure measurement in microsystems using volume displacement of particle suspensions. Lab Chip 9:3345–3353

Cobos S, Carvalho MS, Alvarado V (2009) Flow of oil-water emulsions through a constricted capillary. Int J Multiph Flow 35:507–515

Cooksey GA, Ahmed Z (2016) Optofluidic temperature and pressure measurements with fiber Bragg gratings embedded in microfluidic devices. In: Technical proceedings of the techconnect world innovation conference and expo, Washington, DC

Dinh T, Nguyen TK, Phan HP, Fastier-Wooller J, Tran CD, Nguyen NT, Dao DV (2018) Electrical resistance of carbon nanotube yarns under compressive transverse pressure. IEEE Electron Device L:0741–3106

Dal Dosso F, Tripodi L, Spasic D, Kokalj T, Lammertyn J (2019) Innovative hydrophobic valve allows complex liquid manipulations in a self-powered channel-based microfluidic device. ACS Sens 4:694–703

Douville NJ, Zamankhan P, Tung Y, Li R, Vaughan BL, Tai C, White J, Christensen PJ, Grotberg JB, Takayama S (2011) Combination of fluid and solid mechanical stresses contribute to cell death and detachment in a microfluidic alveolar model. Lab Chip 11:609–619

Eaton WP, Smith JH (1997) Micromachined pressure sensors: review and recent developments. Smart Mater Struct 6:530–539

Escudero P, Yeste J, Pascual-Izarra C, Villa R, Alvarez M (2019) Color tunable pressure sensors based on polymer nanostructured membranes for optofluidic applications. Sci Rep 9:3259

Foland S, Swedlove B, Nguyen H, Lee JB (2012) One-dimensional nanograting-based guided-mode resonance pressure sensor. J Microelectromech Syst 21:1117–1123

Foland S, Liu K, MacFarlane D, Lee J (2011) High-sensitivity microfluidic pressure sensor using a membrane-embedded resonant optical grating. In: Sensors, 2011 IEEE Limerick, Ireland: SENSORS, 2011 IEEE, pp 101–104

Freitas DN, Mongersun A, Chau H, Araci IE (2019) Tunable soft lithography molds enable rapid-prototyping of multi-height channels for microfluidic large-scale integration. J Micromech Microeng 29:35009

Gao Y, Ota H, Schaler EW, Chen K, Zhao A, Gao W, Fahad HM, Leng Y, Zheng A, Xiong F, Zhang C, Tai LC, Zhao P, Fearing RS, Javey A (2017) Wearable microfluidic diaphragm pressure sensor for health and tactile touch monitoring. Adv Mater 29:1701985

Gao J, Yin X, Fang Z (2004) Integration of single cell injection, cell lysis, separation and detection of intracellular constituents on a microfluidic chip. Lab Chip 4:47–52

Garstecki P, Fuerstman MJ, Fischbach MA, Sia SK, Whitesides GM (2006) Mixing with bubbles: a practical technology for use with portable microfluidic devices. Lab Chip 6:207–212

Garstecki P, Gitlin I, DiLuzio W, Whitesides GM, Kumacheva E, Stone HA (2004) Formation of monodisperse bubbles in a microfluidic flow-focusing device. Appl Phys Lett 85:2649–2651

Gervais T, El-Ali J, Gunther A, Jensen K (2006) Flow-induced deformation of shallow microfluidic channels. Lab Chip 6:500–507

Groisman A, Enzelberger M, Quake SR (2003) Microfluidic memory and control devices. Science 300:955–958

Gu W, Zhu X, Futai N, Cho BS, Takayama S (2004) Computerized microfluidic cell culture using elastomeric channels and Braille displays. Proc Natl Acad Sci USA 101:15861–15866

Günther A, Jensen KF (2006) Multiphase microfluidics: from flow characteristics to chemical and materials synthesis. Lab Chip 6:1487–1503

Hardy BS, Uechi K, Zhen J, Kavehpour HP (2009) The deformation of flexible PDMS microchannels under a pressure driven flow. Lab Chip 9:935–938

Hasselbrink EF, Shepodd TJ, Rehm JE (2002) High-pressure microfluidic control in lab-on-a-chip devices using mobile polymer monoliths. Anal Chem 74:4913–4918

Hoera C, Kiontke A, Pahl M, Belder D (2018) A chip-integrated optical microfluidic pressure sensor. Sens Actuators B Chem 255:2407–2415

Hosokawa K, Hanada K, Maeda R (2002) A polydimethylsiloxane (PDMS) deformable diffraction grating for monitoring of local pressure in microfluidic devices. J Micromech Microeng 12:1–6

Hu C, Chen Y, Tan MJA, Ren K, Wu H (2019) Microfluidic technologies for vasculature biomimicry. Analyst 144:4461–4471

Huang C, Gregory JW, Sullivan JP (2007) Microchannel pressure measurements using molecular sensors. J Microelectromech Syst 16:777–785

Huang CY, Lai CM (2012) Pressure measurements with molecule-based pressure sensors in straight and constricted PDMS microchannels. J Micromech Microeng 22:65021

Huang C, Matsuda Y, Gregory JW, Nagai H, Asai K (2014) The applications of pressure-sensitive paint in microfluidic systems. Microfluid Nanofluid 18:739–753

Huang Q, Qin M, Zhou M, Zhou W (2005) A novel capacitive pressure sensor based on sandwich structures. J Microelectromech Syst 14:1272–1282

Huh D, Matthews BD, Mammoto A, Montoya-Zavala M, Hsin HY, Ingber DE (2010) Reconstituting organ-level lung functions on a chip. Science 328:1662–1668

Jin Y, Orth A, Schonbrun E, Crozier KB (2012) Measuring the pressures across microfluidic droplets with an optical tweezer. Opt Express 20:24450–24464

Jung JH, Destgeer G, Ha B, Park J, Sung HJ (2016) On-demand droplet splitting using surface acoustic waves. Lab Chip 16:3235–3243

Jung T, Yang S (2015) Highly stable liquid metal-based pressure sensor integrated with a microfluidic channel. Sensors 15:11823–11835

Kamruzzaman A, Koksal YA, Yin X, Kazemi H, Ozkan E, Kaya NU (2019) Non-invasive pressure sensing in microfluidic chips using laser interferometry. In: Proceedings of the society of photo-optical instrumentation engineers (SPIE), Denver, CO, USA, p 109730M

Khabiry M, Chung BG, Hancock MJ, Soundararajan HC, Du Y, Cropek D, Lee WG, Khademhosseini A (2009) Cell docking in double grooves in a microfluidic channel. Small 5:1186–1194

Kim H, Evans A T, Kim H (2011) A rapid-prototyped on-chip vacuum gauge utilizing the volumetric expansion of trapped air in a sealed microchamber. In: International conference on miniaturized systems for chemistry and life sciences, Seattle, Wash, pp 1119–1121

Kimura F, Khalil G, Zettsu N, Xia Y, Callis J, Gouterman M, Dalton L, Dabiri D, Rodriguez M (2006) Dual luminophore polystyrene microspheres for pressure-sensitive luminescent imaging. Meas Sci Technol 17:1254–1260

Kohl MJ, Abdel-Khalik SI, Jeter SM, Sadowski DL (2005) A microfluidic experimental platform with internal pressure measurements. Sens Actuators A Phys 118:212–221

Laser DJ, Santiago JG (2004) Topical review: a review of micropumps. J Micromech Microeng 14:R35–R64

Lee D, Choi Y (2008) A novel pressure sensor with a PDMS diaphragm. Microelectron Eng 85:1054–1058

Lee H, Chung J, Chang S, Yoon E (2008) Normal and shear force measurement using a flexible polymer tactile sensor with embedded multiple capacitors. J Microelectromech Syst 17:934–942

Li S, Jacobi I, Zeng W, Stone HA, Beck DJ (2015) Characterization of syringe-pump-driven induced pressure fluctuations in elastic microchannels. Lab Chip 15:1110–1115

Li H, Luo CX, Ji H, Ouyang Q, Chen Y (2010) Micro-pressure sensor made of conductive PDMS for microfluidic applications. Microelectron Eng 87:1266–1269

Liao Y, Chen L, Yang G, Liu C (2011) Study of pressure measurement method for micro-fluid chip using laminar flow distribution. Transducer Microsyst Technol 30:80–82

Lissandrello C, Yakhot V, Ekinci KL (2012) Crossover from hydrodynamics to the kinetic regime in confined nanoflows. Phys Rev Lett 108:84501

Liu T, Campbell BT, Burns SP, Sullivan JP (1997) Temperature- and pressure-sensitive luminescent paints in aerodynamics. Appl Mech Rev 50:227–246

Liu M, Shih H, Wu J, Weng T, Wu C, Lu J, Tung Y (2013) Electrofluidic pressure sensor embedded microfluidic device: a study of endothelial cells under hydrostatic pressure and shear stress combinations. Lab Chip 13:1743–1753

Majerus SJA, Garverick SL, Suster MA, Fletter PC, Damaser MS (2012) Wireless, ultra-low-power implantable sensor for chronic bladder pressure monitoring. ACM J Emerg Technol Comput 8:11

Maroufi M, Nikooienejad N, Mahdavi M, Moheimani SOR (2020) SOI-MEMS bulk piezoresistive displacement sensor: a comparative study of readout circuits. J Microelectromech Syst 29:43–53

Martínez-Calvo A, Sevilla A, Peng GG, Stone HA (2020) Start-up flow in shallow deformable microchannels. J Fluid Mech 885:25

Matsuda Y, Misaki R, Yamaguchi H, Niimi T (2011) Pressure-sensitive channel chip for visualization measurement of micro gas flows. Microfluid Nanofluid 11:507–510

Matsuda Y, Mori H, Sakazaki Y, Uchida T, Suzuki S, Yamaguchi H, Niimi T (2009) Extension and characterization of pressure-sensitive molecular film. Exp Fluids 47:1025–1032

Molla S, Eskin D, Mostowfi F (2011) Pressure drop of slug flow in microchannels with increasing void fraction: experiment and modeling. Lab Chip 11:1968–1978

Nakao Y, Kimura H, Sakai Y, Fujii T (2011) Bile canaliculi formation by aligning rat primary hepatocytes in a microfluidic device. Biomicrofluidics 5:22212

Nawi MNM, Manaf AA, Rahman MFA, Arshad MR, Sidek O (2015) One-side-electrode-type fluidic-based capacitive pressure sensor. IEEE Sens J 15:1738–1746

Nguyen TK, Phan HP, Kamble H, Vadivelu R, Dinh T, Iacopi A, Walker G, Hold L, Nguyen NT, Dao DV (2017) Superior robust ultra-thin single crystalline silicon carbide membrane as a versatile platform for biological applications. Acs Appl Mater Inter 9:41641–41647

Nie B, Xing S, Brandt JD, Pan T (2012) Droplet-based interfacial capacitive sensing. Lab Chip 12:1110–1118

Orth A, Schonbrun E, Crozier KB (2011) Multiplexed pressure sensing with elastomer membranes. Lab Chip 11:3810–3815

Ozsun O, Yakhot V, Ekinci KL (2013) Noninvasive measurement of the pressure distribution in a deformable micro-channel. J Fluid Mech 734:R1

Park CS, Kang BS, Lee DW, Choi TY, Choi YS (2007) Fabrication and characterization of a pressure sensor using a pitch-based carbon fiber. Microelectron Eng 84:1316–1319

Park DY, Lee J, Chung JJ, Jung Y, Kim SH (2019) Integrating organs-on-chips: multiplexing, scaling, vascularization, and innervation. Trends Biotechnol 38:99–112

Phan H, Nguyen T, Dinh T, Iacopi A, Hold L, Shiddiky MJA, Dao DV, Nguyen N (2018) Robust free-standing nano-thin SiC membranes enable direct photolithography for MEMS sensing applications. Adv Eng Mater 20:1700858

Prakash M, Gershenfeld N (2007) Microfluidic bubble logic. Science 315:832–835

Quake SR, Scherer A (2000) From micro- to nanofabrication with soft materials. Science 290:1536–1540

Raj MK, Chakraborty J, Dasgupta S, Chakraborty S (2018b) Flow-induced deformation in a microchannel with a non-Newtonian fluid. Biomicrofluidics 12:34116

Raj MK, Dasgupta S, Chakraborty S (2017) Hydrodynamics in deformable microchannels. Microfluid Nanofluid 21:70

Raj MK, Dasgupta S, Chakraborty S (2019) Biomimetic pulsatile flows through flexible microfluidic conduits. Biomicrofluidics 13:14103

Raj A, Sen AK (2016) Flow-induced deformation of compliant microchannels and its effect on pressure–flow characteristics. Microfluid Nanofluid 20:31

Raj A, Suthanthiraraj PPA, Sen AK (2018a) Pressure-driven flow through PDMS-based flexible microchannels and their applications in microfluidics. Microfluid Nanofluid 22:128

Sackmann EK, Fulton AL, Beebe DJ (2014) The present and future role of microfluidics in biomedical research. Nature 507:181–183

Schanze KS, Carroll BF, Korotkevitch S, Morris MJ (1997) Temperature dependence of pressure sensitive paints. AIAA J 35:306–310

Schoch RB, Han J, Renaud P (2008) Transport phenomena in nanofluidics. Rev Mod Phys 80:839–883

Schonbrun E, Abate AR, Steinvurzel PE, Weitz DA, Crozier KB (2010) High-throughput fluorescence detection using an integrated zone-plate array. Lab Chip 10:852–856

Schroeder CM, Babcock HP, Shaqfeh ESG, Chu S (2003) Observation of polymer conformation hysteresis in extensional flow. Science 301:1515–1519

Sekimori Y, Yoshida Y, Kitamori T (2004) Pressure sensor for micro chemical system on a chip. In: Sensors, 2004. Proceedings of IEEE Vienna, Austria, pp 516–519

Setiono A, Bertke M, Nyang' AuWO, Xu J, Fahrbach M, Kirsch I, Uhde E, Deutschinger A, Fantner EJ, Schwalb CH, Wasisto HS, Peiner E (2020) In-plane and out-of-plane MEMS piezoresistive cantilever sensors for nanoparticle mass detection. Sensors 20:618

Shaikh KA, Ryu KS, Goluch ED, Nam J, Liu J, Thaxton CS, Chiesl TN, Barron AE, Lu Y, Mirkin CA, Liu C (2005) A modular microfluidic architecture for integrated biochemical analysis. Proc Natl Acad Sci USA 102:9745–9750

Shen F, Ai M, Ma J, Li Z, Xue S (2020) An easy method for pressure measurement in microchannels using trapped air compression in a one-end-sealed capillary. Micromachines 11:914

Shen F, Li Z, Xue S, Li M, Liu Z (2021) Particle recirculating orbits within microvortices using microfluidics. J Physi D Appl Phys 54:025401

Song W, Psaltis D (2010a) Optofluidic pressure sensor based on interferometric imaging. Opt Lett 35:3604–3606

Song W, Psaltis D (2010b) Imaging based optofluidic air flow meter with polymer interferometers defined by soft lithography. Opt Express 18:16561–16566

Song W, Psaltis D (2011) Optofluidic membrane interferometer: an imaging method for measuring microfluidic pressure and flow rate simultaneously on a chip. Biomicrofluidics 5:44110

Squires TM, Quake SR (2005) Microfluidics: fluid physics at the nanoliter scale. Rev Mod Phys 77:977–1026
Srivastava N, Burns MA (2007) Microfluidic pressure sensing using trapped air compression. Lab Chip 7:633–637
Stone HA, Stroock AD, Ajdari A (2004) Engineering flow in small devices. Annu Rev Fluid Mech 36:381–411
Sun H, Fang D, Jia K, Maarouf F, Qu H, Xie H (2011) A low-power low-noise dual-chopper amplifier for capacitive CMOS-MEMS accelerometers. IEEE Sens J 11:925–933
Suter JD, Hohimer CJ, Fricke JM, Christ J, Kim H, Evans AT (2013) Principles of meniscus-based MEMS gas or liquid pressure sensors. J Microelectromech Syst 22:670–677
Sutera SP, Skalak R (1993) The history of Poiseuille's law. Annu Rev Fluid Mech 25:1–20
Suteria N, Nekouei M, Vanapalli S (2018) Microfluidic bypass manometry: highly parallelized measurement of flow resistance of complex channel geometries and trapped droplets. Lab Chip 18:343–355
Tan Y, Dai D (2018) Silicon microring resonators. J Opt 20:54004
Tang L, Hong W, Wang X, Sun W, Yang B, Wei M, Pan J, Liu J (2019) Ultraminiature and flexible sensor based on interior corner flow for direct pressure sensing in biofluids. Small 15:1900950
Tsai CD, Kaneko M (2016) On-chip pressure sensor using single-layer concentric chambers. Biomicrofluidics 10:24116
Unger MA, Chou HP, Thorsen T, Scherer A, Quake SR (2000) Monolithic microfabricated valves and pumps by multilayer soft lithography. Science 288:113–116
Vanapalli SA, van den Ende D, Duits MHG, Mugele F (2007) Scaling of interface displacement in a microfluidic comparator. Appl Phys Lett 90:114109
Varel C, Shih Y, Otis BP, Shen TS, Bohringer KF (2014) A wireless intraocular pressure monitoring device with a solder-filled microchannel antenna. J Micromech Microeng 24:45011–45012
Walmsley SR (2019) Immune-cell function under pressure. Nature 573:41–42
Wang J, Liu Z, Pang Y, Li M, Zhou Q (2021) Breakup of compound jets with inner droplets in a capillary flow-focusing device. Phys Fluids 33:13304
Wang L, Zhang M, Yang M, Zhu W, Wu J, Gong X, Wen W (2009) Polydimethylsiloxane-integratable micropressure sensor for microfluidic chips. Biomicrofluidics 3:34105
Wheeler AR, Throndset WR, Whelan RJ, Leach AM, Zare RN, Liao YH, Farrell K, Manger ID, Daridon A (2003) Microfluidic device for single-cell analysis. Anal Chem 75:3581–3586
Whitesides GM (2006) The origins and the future of microfluidics. Nature 442:368–373
Whitesides GM, Ostuni E, Takayama S, Jiang X, Ingber DE (2001) Soft lithography in biology and biochemistry. Annu Rev Biomed Eng 3:335–373
Whitesides GM, Stroock AD (2001) Flexible methods for microfluidics. Phys Today 54:42
Witwer KW, Wolfram J (2021) Extracellular vesicles versus synthetic nanoparticles for drug delivery. Nat Rev Mater 6:103–106
Wu K, Li X (2020) Wearable pressure sensor for athletes' full-range motion signal monitoring. Mater Res Express 7:105003
Wu C, Liao W, Tung Y (2011) Integrated ionic liquid-based electrofluidic circuits for pressure sensing within polydimethylsiloxane microfluidic systems. Lab Chip 11:1740–1746
Wu CY, Lu JC, Liu MC, Tung YC (2012) Integrated electrofluidic circuits: pressure sensing with analog and digital operation functionalities for microfluidics. Lab Chip 12:3943–3951
Xu H, Hafezi M, Fan J, Taylor JM, Strouse GF, Ahmed Z (2013) Ultrasensitive chip-based photonic temperature sensor using ring resonator structures. Opt Express 22:3098–3104
Yalikun Y, Ota N, Guo B, Tang T, Zhou Y, Lei C, Kobayashi H, Hosokawa Y, Li M, Muñoz HE, Carlo DD, Goda K, Tanaka Y (2020) Effects of flow-induced microfluidic chip wall deformation on imaging flow cytometry. Cytom A 97:909–920
Yang G, Liao Y, Yang J, Chen L, Zheng X, Hu N (2012) Study on a multi-channel micro fluid chip pressure measurement method based on laminar flow distribution. Chin J Sci Instrum 33:2546–2551
Yu N, Liu Y, Ji B, Wang S, Chen Y, Sun T, Zhang J, Yang B (2020) High-sensitivity microliter blood pressure sensors based on patterned micro-nanostructure arrays. Lab Chip 20:1554–1561
Yu M, Mori H, Niimi T, Uenishi H, Hirako M (2007) Development of pressure sensitive molecular film applicable to pressure measurement for high Knudsen number flows. Exp Fluids 42:543–550
Zhang Q, Lei J, Chen Y, Wu Y, Xiao H (2020) Glass 3D printing of microfluidic pressure sensor interrogated by fiber-optic refractometry. IEEE Photonic Technol Lett 32:414–417
Zhao X, Yan X, Li Y, Liu B (2019) Static pressure-driven microfluidic gradient generator for long-term cell culture and adaptive cytoprotection analysis. Microfluid Nanofluid 23:62
Zhou X, Zhang R, Li L, Zhang L, Liu B, Deng Z, Wang L, Gui L (2019) A liquid metal based capacitive soft pressure microsensor. Lab Chip 19:807–814